Submitted to International Journal of Architectural Heritage

Meta-model assisted continuous vibration-based damage identification of a historical rammed earth tower in the Alhambra complex

García-Macías, E.[a], Hernández-González, I. A.[a], Puertas, E.[a], Gallego, R.[a], Castro-Triguero, R.[b], and F. Ubertini[c]

[a]Department of Structural Mechanics and Hydraulic Engineering, University of Granada, Av. Fuentenueva sn, 18002 Granada, Spain.
[b]Department of Mechanics, University of Córdoba, Spain.
[c]Department of Civil and Environmental Engineering, University of Perugia. Via G. Duranti, 93 - 06125 Perugia, Italy.

ABSTRACT
This work presents the development of a model-based online damage identification system for a 13th century rammed earth (RE) tower in the Alhambra, the Muhammad Tower. The system is fed with continuous data from an ambient vibration-based monitoring system and a meteorological station. Ambient vibrations are continuously processed through Operational Modal Analysis (OMA), and environmental effects are minimised via statistical pattern recognition. The normalized modal signatures are used to update the stiffness properties of certain parts of the tower through inverse model calibration. To do so, a high-fidelity three-dimensional finite element model (FEM) of the tower is developed. Since its computational burden precludes conducting online calibration, the FEM is bypassed by a light Kriging surrogate model (SM). In this light, the developed SM-assisted system identification constitutes a long-term Structural Health Monitoring (SHM) system outputting quasi-real-time series of modal properties and local stiffness parameters, so providing full damage assessment (detection, localization and quantification). The presented results refer to a time period of three months since January until March 2022. Numerical results and discussion are reported concerning the characterization and removal of environmental effects, and synthetic damage scenarios through non-linear simulations are used to validate the developed damage identification system.

KEYWORDS
Automated OMA; Architectural heritage; Damage assessment; Historical construction; Model Updating; Statistical Pattern Recognition; Structural Health Monitoring; Surrogate modelling

1. Introduction

Raw earth has been used worldwide for millennia as a traditional construction material, and nowadays earthen architecture is attracting growing interest as a viable solution for modern sustainable building policies (Bernardo et al. (2022)). The most ancient use of this material dates back to 10,000 B.C.E. as evidenced by archaeological excavations of the first permanent dwellings in South-west Asia (Schroeder

Corresponding author García-Macías, E. Email: enriquegm@ugr.es

(2016)). The most widespread construction techniques with raw earth are adobe masonry and RE (Minke (2013)). Adobes are sun-dried mud bricks typically layered with earth mortar, while RE consists in compacting moistened earth inside a form-work to erect walls. Rammed earth construction has a particularly long tradition in Spain and Portugal, where it prospered during the Islamic occupation of the Iberian Peninsula between the 8$^{\text{th}}$ and the 15$^{\text{th}}$ centuries (Jaquin et al. (2007); Jiménez-Delgado and Guerrero (2006)). Noticeable examples are the historic centre of the city of Córdoba, or the Alhambra, Generalife and Albayzín in Granada, enlisted by UNESCO as World Heritage Sites (WHSs) (Viu et al. (2008)). Given their strategic role in the tourism industry and related sectors as well as their invaluable historical, architectural and artistic value, there exists broad awareness among citizens and administrations on the critical importance of safeguarding these Cultural Heritage (CH) structures. Nonetheless, although the implementation of SHM to civil engineering infrastructures such as bridges or dams is becoming popular, the application to CH structures and specially to RE constructions remains marginal.

In the broadest sense, SHM exploits long-term monitoring data to track anomalies in the structural performance caused by damage and, desirably, to predict damage evolution and structural life expectancy (Boller et al. (2009)). Among the wide variety of available technologies, ambient vibration-based SHM has become particularly popular for CH structures owing to their non-destructive nature and minimum intrusiveness, causing no disruption to the normal fruition of the monitored assets (Carden and Fanning (2004); Pallarés et al. (2021)). These systems are often complemented with sensors assessing the environmental and operational conditions (EOC) to facilitate the discrimination of damage effects from normal fluctuations in the in-service structural performance. Environmental effects typically translate into daily and seasonal trends in the dynamic response of the monitored structure, which may mask the appearance of structural pathologies and thus need to be filtered out through pattern recognition (Farrar and Worden (2012)). In this regard, a noticeable evidence is the well-known benchmark case study of the Z24-Bridge in Switzerland first reported by Peeters and De Roeck (2001), who found variations of up to 18% in the first four resonant frequencies of the bridge primarily driven by temperature oscillations. In general, field applications reported in the literature reveal that the effects of EOC are extremely case-dependent. In masonry structures, positive correlations between environmental temperature and resonant frequencies are often observed (see e.g. Ceravolo et al. (2021); Ubertini et al. (2018)). Such a behaviour is commonly ascribed to the closure of surface- or micro- cracks induced by thermal expansion with the subsequent stiffening effect. Nevertheless, completely different correlations can be found depending on the structural topology, solar radiation, material heterogeneity, and more. For instance, Gentile et al. (2019) reported negative correlations between temperature and the resonant frequencies of the Milan Cathedral (Italy). The combination of static and dynamic monitoring allowed those authors to conclude that such a correlation was driven by the actions exerted by metallic tie-rods in the cathedral. Similarly, García-Macías and Ubertini (2022b) reported negative correlations between environmental temperature and the resonant frequencies of a masonry palace in Gubbio (Italy), the Consoli Palace. In that case, such correlations were ascribed to temperature-induced softening of some metallic tie rods restraining the lateral thrusts exerted by the barrel-vault ceiling of the palace.

While most research on condition-based maintenance of CH assets focuses on masonry constructions, the number of experiences on continuous SHM of earthen architecture is considerably more scarce. Among the few works in the literature, it is worth noting the contribution by Miccoli et al. (2017) who reported an experimental campaign carried out for a time period of 13 months to evaluate the structural vulnerability of a medieval earthen building at Ambel (Zaragoza, Spain). The potential presence of active damage mechanisms was surveyed with a static monitoring system comprising linear variable displacement transducers (LVDTs) and digital strain gauges across major cracks in the façades of the building. Correlation analyses with environmental factors (temperature and humidity) allowed those authors to conclude that the monitored crack displacements were reversible and solely driven by daily and seasonal EOC, thus discarding the existence of active damage mechanisms. In general, negative correlations between crack displacements and temperature were observed – decreasing temperature induces material contraction with the subsequent crack opening. Another noteworthy contribution was made by Aguilar et al. (2019) who reported the continuous ambient-vibration monitoring of the 16th century adobe Church of San Pedro Apóstol in Andahuaylillas (Peru) from March 2017 to December 2018. Their results evidenced the existence of positive and negative correlations between the resonant frequencies of the church with environmental temperature and humidity, respectively. With the aim of assessing the potential appearance of damage after a 5.2 Mw earthquake occurred in October 2018 and with epicenter 110.8 km far from the church, those authors eliminated the effects of ECO through and Autoregressive model with Exogenous (ERX) input and Principal Component Analysis (PCA). In agreement with visual inspections and the low ground-motions registered on site, the filtered time series of modal signatures proved no anomaly indicating the appearance of structural damage.

The damage identification problem is commonly organized in a hierarchical structure of increasing complexity (Rytter (1993)): Level I: Detection; Level II: Localization; Level III: Classification; Level IV: Extension; and Level V: Prognosis. On this basis, damage assessment can be generally conducted by means of unsupervised learning (UL) and supervised learning (SL) tools (Hou and Xia (2021)). Unsupervised techniques through statistical pattern recognition and anomaly detection have become particularly popular given its independence from structural models and related uncertainties, as well as its straightforward implementation into continuous SHM schemes (de Oliveira Dias Prudente dos Santos et al. (2016); Martinez-Luengo et al. (2016); García-Macías and Ubertini (2022a)). Nonetheless, a major drawback of UL regards its limitation to damage detection (Level I), being possible to locate and quantify defects only in some particular cases. Although this can suffice for the maintenance of singular CH constructions, SL techniques allowing higher damage identification levels may become imperative for the management of architectural ensembles and the coordination of field inspections with emergency services after natural disasters such as earthquakes. These techniques, often referred to as Structural Identification (St-Id), represent the process of construction and inverse calibration of a mathematical model of a structural system through observations and experimental data, which can be used for estimations and predictions of increased confidence on the condition and residual life of structural systems (Lai et al. (2021)). The calibration of such models is typically conducted through model updating approaches. Model updating aims to bridge the gap between numerical models and real systems by tuning the model parameters in such a way that the mismatch amidst experimental and theoretical observations is minimal (Alkayem et al. (2018)). The progressive cheapening of sensor technologies (Mishra et al. (2022)) and the hasty development of machine learning (ML) and artificial intelligence (AI) (Mishra (2021)) in recent years have enabled the incorporation of SL approaches to the novel concept of Digital Twins (Chakraborty et al. (2021); Chiachío et al. (2022)). In general, a digital twin (DT) represents a digital replica of a physical asset characterized by cyber-physical interaction (Tao et al. (2018)). In the context of SHM of civil engineering structures, a DT involves a physics-based or a machine learning model that continuously exploits monitoring data to infer and classify the health condition of the physical asset (Angjeliu et al. (2020)). In this light, a growing number of recent publications can be found in the literature on the development of continuous deterministic (Cabboi et al. (2017); García-Macías et al. (2020)) and probabilistic (García-Macías and Ubertini (2022c); Zhou et al. (2022)) model updating approaches capable of providing real-time damage identification.

In the realm of RE historic constructions, most research efforts in the literature have focused on the development of efficient seismic vulnerability assessment techniques. It is worth noting the work by Silva et al. (2018) who proposed a general classification method for the vulnerability assessment of twenty traditional Portuguese RE dwellings based on simple geometrical and seismic hazard indexes. In addition, a set of destructive and non-destructive tests for more precise classifications were also proposed and applied to a modern RE building in Esposende, northern Portugal. Considerable efforts have been also devoted to the modelling of RE historic constructions. This represents a formidable problem given the complex constitutive properties of RE (Ávila et al. (2022a)) and the intrinsic uncertainties of any ancient structure (uncertain history of interventions, pre-existing pathologies, material heterogeneity, to mention a few). Smeared damage approaches based on the concrete damage plasticity (CDP) constitutive law have proved efficient to simulate the non-linear behaviour of adobe (Al Aqtash et al. (2017)) and RE structures (Bui et al. (2020)). Following this approach, Nguyen et al. (2021) evaluated different modelling strategies to replicate the seismic response of an inner-reinforced RE building under shaking table tests conducted by Zhou and Liu (2019). Their results evidenced the importance of implementing 3D volume elements to achieve close fittings with the experimental data. Another noteworthy contribution on the modelling of full-scale RE assets is the one by Martínez et al. (2022) who reported the development of a 3D FEM of the 13$^{\text{th}}$ century Tower of Comares in the Alhambra, Granada (Spain). Given the massive nature of this sort of constructions and the considerable material heterogeneity stemming from diverse interventions over centuries, those authors evidenced the importance of implementing 3D elements to account for an accurate definition of volumes and material distribution. In particular, after a detailed material and geometrical survey, those authors considered 12 structural partitions and 9 different material models in the FEM of the tower. The seismic vulnerability of another prominent tower in the Alhambra, the Torre de la Vela, was also recently investigated by Vuoto et al. (2022) through non-linear static simulations. For that purpose, those authors developed a high-fidelity 3D FEM of the tower exploiting a comprehensive on-site survey involving laser scanning, sonic tests, and an ambient vibration test (AVT).

It is clear from the literature review above that the numerical modelling of historic RE constructions is typically computationally intensive, which represents a major obstacle for the implementation of St-Id into automated long-term SHM systems. In this light, this work presents the development of a SM-assisted online damage identification system for a 13$^{\text{th}}$-century RE tower in the Alhambra monumental complex, the Muhammad Tower. The present investigation is framed within a research project aimed at assessing the structural damage experienced by the tower after a seismic swarm occurred from February until August 2021. In this context, a vibration-based SHM system was installed, comprising 8 uni-axial high-sensitivity piezoelectric accelerometers deployed at the three main levels of the tower and acquiring ambient vibrations continuously since January until March 2022. On this basis, the modal properties of the tower are continuously extracted by automated Operational Modal Analysis (OMA), and the presence of benign EOC is characterized with environmental data from an adjacent meteorological station and minimised via statistical pattern recognition. Then, the normalized time series of modal signatures are used to infer the local stiffness distribution in the tower through physics-based St-Id. To do so, a high-fidelity three-dimensional FEM is developed accounting for the complex distribution of volumes in the structure. Since the computational burden of the 3D FEM precludes its direct use for online inverse calibration, it is bypassed by a light meta-model. To this aim, a Kriging SM is constructed to map the selected stiffness parameters and the modal signatures of the tower. The developed SM-assisted St-Id approach constitutes a long-term SHM system outputting quasi-real-time series of global modal properties and local stiffness parameters, so providing full damage assessment (detection, localization and quantification). The presented results first concern the characterization and removal of environmental effects upon the modal properties of the tower. Then, synthetic damage scenarios obtained through non-linear static simulations are used to demonstrate the effectiveness of the proposed methodology.

The remainder of this paper is organized as follows. Section 2 describes the investigated CH construction, the Muhammad Tower, as well as the SHM system installed in the tower. Section 3 presents the proposed meta-model assisted St-Id approach. Sections 4 and 5 overview the theoretical background of automated OMA and Kriging meta-modelling, respectively. Section 6 presents the numerical results and discussion and, finally, Section 7 concludes the paper.

2. Muhammad Tower: Description of the structure and monitoring system

The Muhammad Tower in Fig. 1 (a,c), also referred to as the Hontiveros Tower and the Tower of the Hens (English translation of its Spanish name, Torre de las gallinas), is the westernmost tower of the monumental complex of the Alhambra (Fig. 1 (b)), which is currently one of the few preserved palatine cities of the medieval Islamic period in Europe (8^{th}-15^{th} centuries). The Alhambra overlooks the city of Granada (Andalusia) on top of the Sabika Hill at the foot of the Sierra Nevada Mountains in South-East Spain (see Fig. 1 (b)). Originally constructed as a military enclosure, the Alhambra became a fortified palatine city during the Nasrid dynasty in the mid-13^{th} century. Designated as a world heritage site by UNESCO in 1984, the Alhambra monumental complex is the second most visited monument in Spain and attracts more than 3 million tourists every year.

Inserted in the walls of the Alhambra Fortress between the Tower of the Cube and the Mexuar Palace, the Muhammad Tower was erected in the 13^{th}-century by Muhammad II to control the access to the royal palaces. The tower has an approximately rectangular cross-section (6.6 $\times$ 9.0 m) composed of 1.3-1.9 m thick RE and brick masonry walls. Along its height, the tower has two vaulted floors (average thickness of 1.65 m) and a terrace rising 11.6 m above the foundation, including a 0.80 m tall parapet and 1.2 m tall battlements (Fig. 1 (d)). The three levels of the tower are connected by masonry staircases at the South-West façade of the tower. The foundations lay on a geological formation of conglomerates with intercalated sands and clays of the Pliocene and Lower Pleistocene, known as the Alhambra Formation. Although there are evidences of numerous modifications of the tower over the centuries, it is only after the 50s that rehabilitation interventions start being documented. These include the underpinning and consolidation of the foundations of the tower by the architect Francisco Prieto-Moreno Pardo in 1975 to rehabilitate the tower after a long period of abandonment in the 19th century.

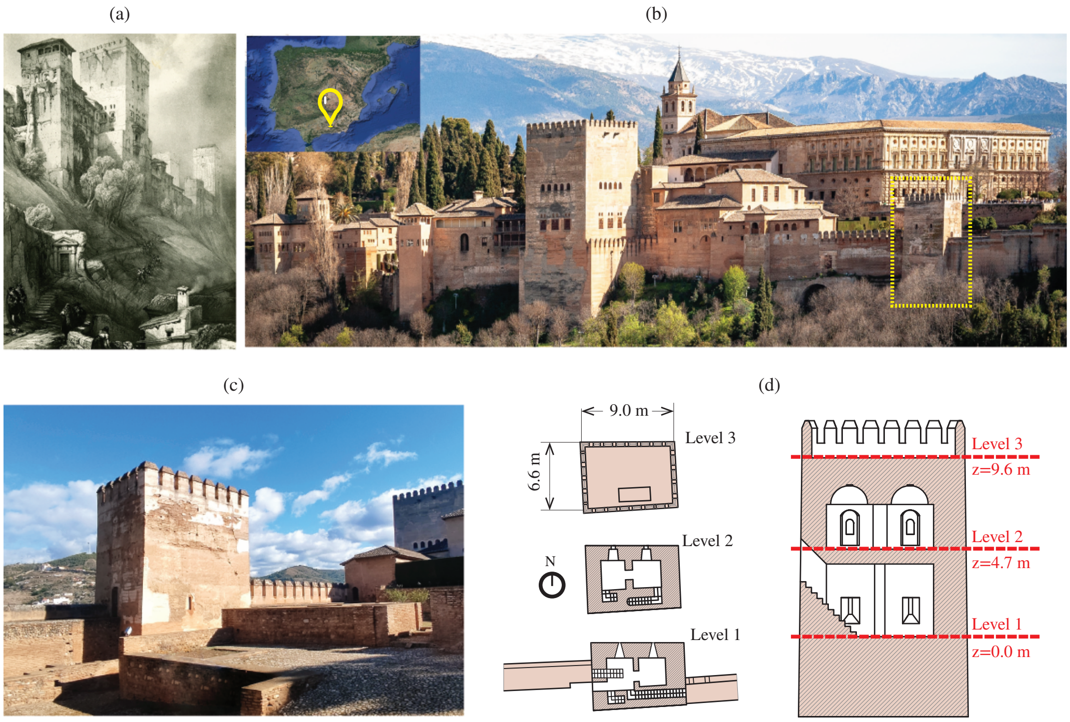

Figure 1. Drawing of the fortress of the Alhambra by David Roberts 1835 (from the Library of the Patronato of the Alhambra and Generalife) (a). Panoramic view of the Alhambra and its geographic position (b). View of the Muhammad Tower (c), plan and elevation views (d).

The present investigation is framed within a research project aimed at assessing the seismic vulnerability of the tower after a seismic swarm occurred from February until August 2021. The seismic sequence registered more than 3,000 events with epicentres only about 20-30 km far from the Alhambra and Mw magnitudes ranging between 0.2 and 4.5. Preliminary in-situ inspections revealed the existence of important earthquake-induced pathologies in the tower, including the extension of some pre-existent major cracks and the appearance of new local defects. In particular, severe damage was detected at the connections of the battlements and the parapet in the top level of the tower, requiring the installation of a temporary underpinning system. With the aim of assessing the current condition of the main body of the tower, a continuous vibration-based SHM system has been installed since January 2022. The monitoring system comprises 8 high-sensitivity piezoelectric accelerometers model PCB393B31 (µ5% 10.0 V/g, broadband Resolution: 1 µg rms and ±0.5 g pk) installed on the three main levels of the tower as shown in Fig. 2 (a). The sensors, labelled with A1 to A8, were mounted on heavy steel plates inside IP66 sealed enclosures laying directly on the floor. The accelerometers are deployed forming a biaxial station in the East façade and a mono-axial one in the North façade (except for the first level where only a bi-axial station is installed). Such a configuration was defined from the authors' experience, the inspection of a preliminary FEM of the tower, and the need for locating the sensors inside the tower where they are not visible by the visitors. This sensors layout is aimed at characterizing the rigid diaphragm motions of the floors and the global torsional rotations of the tower. Ambient vibrations are sampled at 200 Hz and stored in separate data files containing 30-min-long records through the LMS Testxpress software (Siemens, Munich, Germany). The acceleration signals are recoded by a data acquisition system (DAQ) model LMS SCADAS located in the second level, and a portable WiFi router is used for data transfer and remote control of the system. The SHM system was powered by the electric grid of the Alhambra, so no batteries or backup system was provisioned. Environmental data are retrieved from the Granada-Albayzín meteorological station managed by the Department of Mineralogy and Petrology from the University of Granada, located only 280 m far from the tower. Environmental data include air temperature, relative humidity, wind speed, and atmospheric pressure with an acquisition frequency of 10 min.

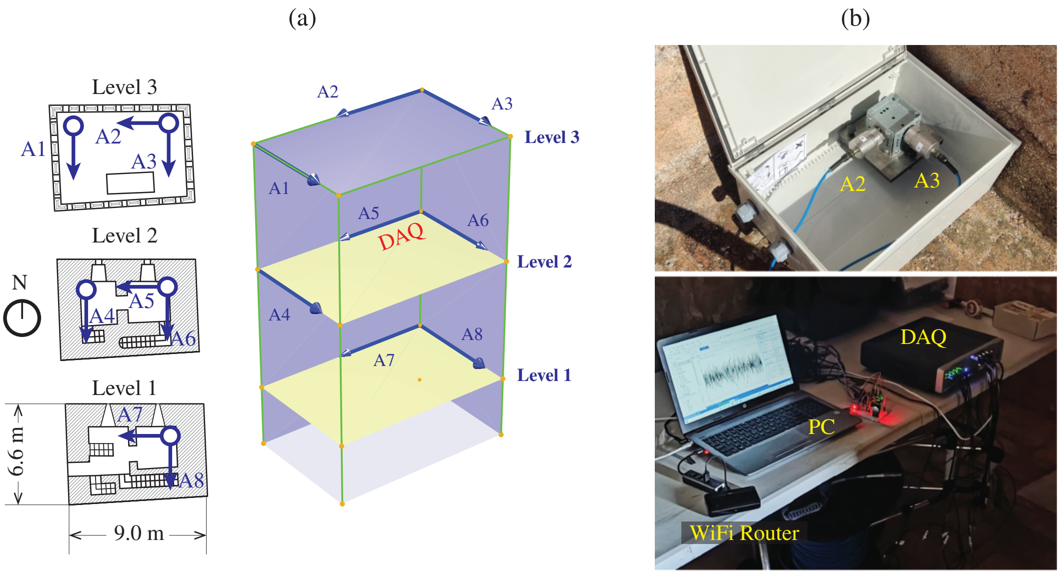

Figure 2. Layout of the continuous monitoring system (a) and views of the sensors and the DAQ equipment (b).

3. Meta-model assisted online damage identification

The work-flow of the implemented meta-model assisted continuous St-Id approach is sketched in Fig. 3. The process iteratively acquires experimental data from the physical asset, conducts St-Id by inverse calibration of the FEM through a meta-model, and identifies the potential presence of damage. To attain quasi-real-time damage identification, it is of pivotal importance to guarantee that the total computational time involved in the signal processing, inverse calibration of the FEM, and the damage assessment is lower than the acquisition time (30 minutes in this work). If so, at any step $j+1$, the damage identification can be conducted in parallel with the previous acquisition j without accumulating time delays. In this light, the procedure comprises four consecutive steps:

(A) *Automated OMA* – Ambient vibrations are periodically recorded by a DAQ and stored in separate data files containing a certain time duration. Then, a set of modal signatures (resonant frequencies f_j, mode shapes φ_j, and damping ratios ζ_j) is extracted through automated OMA.

(B) *Removal of EOC* – The presence of benign fluctuations driven by EOC in the previously identified modal signatures is minimized through statistical pattern recognition.

(C) *SM-assisted St-Id* – This step relates the St-Id of the asset through the model updating of the FEM. This is accomplished by solving a certain optimization problem with an objective function $J(\mathbf{x})$ accounting for the mismatch between the theoretical predictions of the model and the previously identified experimental modal signatures. As a result, certain damage-sensitive model parameters $\mathbf{x}$ are calibrated ($\hat{\mathbf{x}}$) and collected in an observation matrix $\hat{\mathbf{X}}$.

(D) *Damage identification* – Finally, the appearance of structural damage can be appraised by novelty analysis of the time series of modal signatures and model parameters contained in $\hat{\mathbf{X}}$. Since the latter are defined according to certain structural elements or damage mechanisms, the identification of permanent variations in their time series provides direct assessment of the location and severity of the damage.

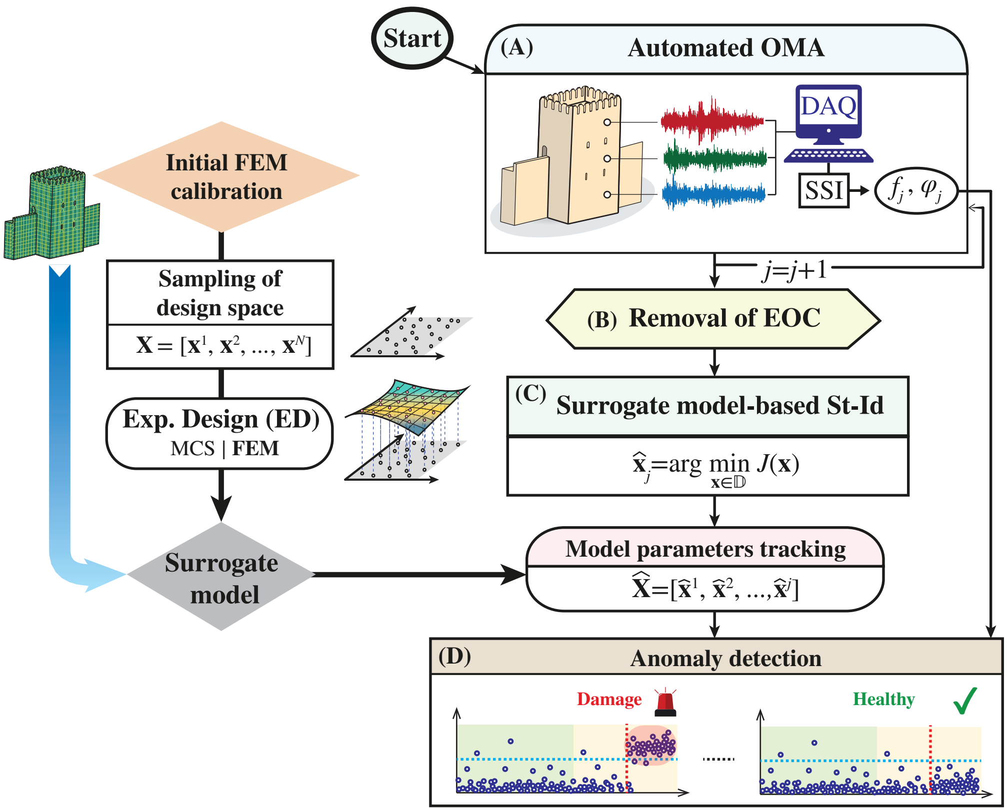

Figure 3. Flowchart of the implemented SM-assisted continuous St-Id of historic buildings.

In order to perform the meta-model assisted St-Id, an objective function $J(\mathbf{x})$ including the relative differences between the l target modes of vibration determined experimentally and their theoretical counterparts is introduced as follows (García-Macías et al. (2020); García-Macías et al. (2021)):

$$J(\mathbf{x}) = \sum_{i=1}^{l} \left[\eta_{(1,i)} \varepsilon_i(\mathbf{x}) + \eta_{(2,i)} \delta_i(\mathbf{x}) \right] + \mathcal{R}(\mathbf{x}), \tag{1}$$

with

$$\varepsilon_i(\mathbf{x}) = \frac{|f_i^{\exp} - f_i^{\mathrm{srr}}(\mathbf{x})|}{f_i^{\exp}}, \quad \delta_i(\mathbf{x}) = 1 - MAC\left(\varphi_i^{\exp}, \varphi_i^{\mathrm{srr}}(\mathbf{x})\right), \tag{2}$$

and $\eta_{(1,i)}$ and $\eta_{(2,i)}$ being weighting coefficients that scale the contribution of the first two terms of the objective function. Terms $f_i^{\exp}$ and $f_i^{\mathrm{srr}}(\mathbf{x})$ denote the i-th resonant frequencies obtained by OMA and by the surrogate model, respectively, while MAC stands for the Modal Assurance Criterion (MAC) between the i-th experimental $\varphi_i^{\exp}$ and theoretical $\varphi_i^{\mathrm{srr}}(\mathbf{x})$ mode shapes. On this basis, the St-Id procedure is given by the following constrained non-linear minimization problem:

$$\hat{\mathbf{x}} = \arg\min_{\mathbf{x}\in\mathbb{D}} J(\mathbf{x}). \tag{3}$$

The last term in Eq. (1), $\mathcal{R}(\mathbf{x})$, represents a regularization term used to mitigate ill-conditioning in the St-Id. In this work, a variation of the classical Tikhonov regularization is introduced as follows:

$$\mathcal{R}(\mathbf{x}) = \frac{1}{m} \sum_{i=1}^{m} \eta_{(3,i)} \frac{\left(x_i - x_i^0\right)^2}{b_i - a_i}, \tag{4}$$

where terms a_i and b_i denote the limits of the allowed range of variation of model parameter x_i, i.e. $a_i \leq x_i \leq b_i$, and term $\eta_{(3,i)}$ represents a trade-off parameter used to weigh the intensity of the regularization for every model parameter. The implemented regularization forces the solution to remain close to a reference vector of design variables $\mathbf{x}^0 = \left[x_1^0, ..., x_m^0\right]^{\mathrm{T}}$ denoting the undamaged condition. For small values of $\eta_{(3,i)}$, the design variable x_i remains almost unrestricted, while too large values may over-constrain the variation of x_i. Note that the aim of defining different trade-off parameters $\eta_{(3,i)}$ for each model parameter is to tackle the particular sensitivities of the modal features to variations in the model parameters. Finally, it is important to remark that the optimization problem in Eq. (3) is often non-convex, thereby global optimization algorithms are recommended to prevent the optimization from getting stuck at local minima.

4. Modal identification and data normalization

4.1. Automated Covariance-driven Stochastic Subspace Identification (Cov-SSI)

The dynamic equilibrium equations of a linear time-invariant system with n_2 degrees of freedom (DOFs) under white noise unmeasured excitation can be written in discrete-time state-space form assuming zero-order hold (ZOH) discretization as (Juang (1994)):

$$\begin{aligned} \mathbf{x}_{(k+1)} &= \mathbf{A}\mathbf{x}_{(k)} + \mathbf{w}_{(k)}, \\ \mathbf{y}_{(k)} &= \mathbf{C}\mathbf{x}_{(k)} + \mathbf{v}_{(k)}, \end{aligned} \tag{5}$$

where $k \in \mathbb{N}$ is a generic time step (i.e. $t\,(k) = k\,\Delta t = k/f_s$ with $f_s = \Delta t^{-1}$ the sampling frequency), and matrices $\mathbf{A} \in \mathbb{R}^{2n_2 \times 2n_2}$ and $\mathbf{C} \in \mathbb{R}^{n_o \times 2n_2}$ respectively denote the state and output matrices of the system, n_o being the number of DOFs monitored by sensors. Vectors $\mathbf{x} \in \mathbb{R}^{2n_2}$ and $\mathbf{y} \in \mathbb{R}^{n_o}$ stand for the state and observation vectors. Vectors $\mathbf{w}_{(k)} \in \mathbb{R}^{2n_2}$ and $\mathbf{v}_{(k)} \in \mathbb{R}^{n_o}$ stand for zero-mean realizations of white noise processes accounting for the unmeasured input forces and the measurement noise, respectively. It can be demonstrated that the structure's natural frequencies ω_i, damping ratios ζ_i and complex mode shapes $\boldsymbol{\varphi}_i$ can be extracted from the eigenvalues μ_i and eigenvectors $\boldsymbol{\phi}_i$ of matrix $\mathbf{A}$ as (Peeters (2000)):

$$\lambda_i = \frac{\ln(\mu_i)}{\Delta t} \Leftrightarrow \lambda_i = -\zeta_i\omega_i + \mathrm{i}\omega_i\sqrt{1-\zeta_i^2}, \quad \boldsymbol{\varphi}_i = \mathbf{C}\,\boldsymbol{\phi}_i, \tag{6}$$

with $\mathrm{i} = \sqrt{-1}$ being the imaginary unit.

On this basis, the Cov-SSI method identifies the stochastic model in Eq. (5) by processing the output covariance matrix of the system. To do so, this method exploits a fundamental property of stochastic discrete-time state-space models relating the correlations between measurement records and the system matrices as $\mathbf{R}_j = \mathbf{C}\mathbf{A}^{j-1}\mathbf{G}$ (Van Overschee and De Moor (2012)), with $\mathbf{R}_j \in \mathbb{R}^{(n_o \times n_o)}$ being the output correlation matrix for a time lag $\tau = j\Delta t$, and $\mathbf{G} \in \mathbb{R}^{(2n_2 \times n_o)}$ the next state-output covariance matrix given by $\mathbf{G} = \mathbb{E}\left[\mathbf{x}_{(k+1)}\mathbf{y}_{(k)}^{\mathrm{T}}\right]$. In this light, the Cov-SSI method decomposes the output correlation matrices $\mathbf{R}_1$ to $\mathbf{R}_{(2j_b-1)}$ for positive time lags varying from Δt to $(2j_b - 1)\Delta t$ and organized into a $n_o\,j_b \times n_o\,j_b$ block Toeplitz matrix as:

$$\mathbf{T}_{1|_{j_b}} = \begin{bmatrix} \mathbf{R}_{j_b} & \mathbf{R}_{j_b-1} & \dots & \mathbf{R}_1 \\ \mathbf{R}_{j_b+1} & \mathbf{R}_{j_b} & \dots & \mathbf{R}_2 \\ \dots & \dots & \dots & \dots \\ \mathbf{R}_{2j_b-1} & \mathbf{R}_{2j_b-2} & \dots & \mathbf{R}_{j_b} \end{bmatrix} = \begin{bmatrix} \mathbf{C} \\ \mathbf{C}\mathbf{A} \\ \dots \\ \mathbf{C}\mathbf{A}^{j_b-1} \end{bmatrix} \begin{bmatrix} \mathbf{A}^{j_b-1}\mathbf{G} & \dots & \mathbf{A}\mathbf{G} & \mathbf{G} \end{bmatrix} = \mathbf{O}\boldsymbol{\Gamma}, \tag{7}$$

where terms $\mathbf{O}$ and $\boldsymbol{\Gamma}$ are the so-called extended observability and reversed extended stochastic controllability matrices, respectively. Then, if the Singular Value Decomposition (SVD) of the block Toeplitz matrix is calculated as:

$$\mathbf{T}_{1|_{j_b}} = \mathbf{U}\mathbf{S}\mathbf{V}^{\mathrm{T}} = \begin{bmatrix}\mathbf{U}_1 & \mathbf{U}_2\end{bmatrix} \begin{bmatrix}\mathbf{S}_1 & \mathbf{0} \\ \mathbf{0} & \mathbf{0}\end{bmatrix} \begin{bmatrix}\mathbf{V}_1^{\mathrm{T}} \\ \mathbf{V}_2^{\mathrm{T}}\end{bmatrix} = \mathbf{U}_1\mathbf{S}_1\mathbf{V}_1^{\mathrm{T}}. \tag{8}$$

the comparison of Eqs. (7) and (8) reveals that the observability and the controllability matrices can be obtained from the outputs of the SVD as:

$$\mathbf{O} = \mathbf{U}_1\mathbf{S}_1^{1/2}, \quad \mathbf{\Gamma} = \mathbf{S}_1^{1/2}\mathbf{V}_1^{\mathrm{T}}. \tag{9}$$

Note in Eq. (8) that only a subset of n singular values from $\mathbf{S}$ are retained in $\mathbf{S}_1$, which is referred to as the model order. Once matrices $\mathbf{O}$ and $\mathbf{\Gamma}$ are obtained, the identification of the state-space matrices is straightforward. On one hand, matrix $\mathbf{C}$ can be extracted from the first n_o rows of the observability matrix. On the other hand, the state matrix $\mathbf{A}$ can be obtained by the Balanced Realization (BR) method first proposed by Kung (1978), which exploits the shift structure of the observability matrix as:

$$\mathbf{A} = \begin{bmatrix} \mathbf{C} \\ \mathbf{CA} \\ \dots \\ \mathbf{CA}^{j_b-2} \end{bmatrix}^{\dagger} \begin{bmatrix} \mathbf{C} \\ \mathbf{CA}^2 \\ \dots \\ \mathbf{CA}^{j_b-1} \end{bmatrix} = \mathbf{O}^{to^{\dagger}}\mathbf{O}^{bo}, \tag{10}$$

where $\mathbf{O}^{to}$ and $\mathbf{O}^{bo}$ contain the first and the last $n_o(j_b - 1)$ rows of $\mathbf{O}$, respectively, and symbol † stands for the Moore-Penrose pseudo-inverse.

The Cov-SSI algorithm is controlled by two parameters to be defined by the user: (i) the model order n given by the number of SVs retained in $\mathbf{S}_1$, and (ii) the time-lag parameter j_b. The value of j_b is typically fixed by the rule of thumb $2j_b \geq f_s/f_o$ (Reynders and De Roeck (2008)), with f_o being the fundamental frequency of the system. Instead, the model order n is iteratively selected spanning a certain interval from n_{min} to n_{max} (at least twice the number of expected modes). Then, with the aim of discriminating between physical and spurious modes, the identified poles are filtered by the application of a set of hard criteria (HC) and soft criteria (SC). The HC criteria concern the elimination of complex conjugate poles, damping ratios above physically feasible values (ζ_{max}), low Mode Phase Collinearity (MPC) values, and high Mode Phase Deviation (MPD) values. After applying HC, a list of stable poles is obtained by imposing tolerances between consecutive model orders, including relative variations of resonant frequencies Δf, damping ratios $\Delta\zeta$, and MAC values. Once a list of stable poles are selected and represented in a stabilization chart, physical modes can be identified in the shape of columns of stable poles. Such a process, however, requires to be automated for its implementation into continuous SHM. In this work, a hierarchical clustering approach similar to the one proposed by Zini et al. (2022) is implemented following six sequential steps:

(i) The algorithm starts ($k = 1$) by considering all the poles λ_i identified for the highest model order n_{max} as single element clusters.
(ii) The process continues by comparing the stable poles obtained between every two consecutive model orders. Let us denote with $f_{[\lambda_i^{(k)}]}$ and $\boldsymbol{\varphi}_{[\lambda_i^{(k)}]}$ the i-th

frequency and mode shape computed from a pole $\lambda_i^{(k)}$ identified at an arbitrary k-th step, respectively. On this basis, the distance d_{ij}^k between the stable poles obtained for the model order n_k and those identified for the immediately lower model order $n_{(k-1)}$ is computed as:

$$d_{ij}^k = (1-\eta)\frac{\left|f_{\left[\lambda_i^{(k)}\right]} - f_{\left[\lambda_j^{(k-1)}\right]}\right|}{f_{\left[\lambda_j^{(k-1)}\right]}} + \eta\left(1 - MAC\left(\boldsymbol{\varphi}_{\left[\lambda_i^{(k)}\right]}, \boldsymbol{\varphi}_{\left[\lambda_j^{(k-1)}\right]}\right)\right), \tag{11}$$

η being a weighting factor between the contributions of Δf and MAC.

(iii) Once all the distances are calculated, the minimum distances d_i^k in Eq. (11) computed between every two consecutive model orders are collected in a vector $\mathbf{d}^k = \left[d_1^k \; d_2^k \; \ldots\right]$.

(iv) The cut-off threshold is estimated as the 80th percentile of the statistical distribution of the distances in $\mathbf{d}^k$.

(v) The Π-shape hierarchical tree (dendogram) is formed according to d_i^k, and the optimal cut-off threshold is used to cut the tree arranging the stable poles in clusters. Low-dimension clusters are filtered out by imposing a minimum number of poles required to form a physical cluster.

(vi) The physical modes are finally defined as the centroids of the previously selected clusters.

4.2. Data normalization

As anticipated above, it is fundamental to minimize the masking effects of EOC to attain effective damage identification. In practice, EOC effects are typically more evident in resonant frequencies, while mode shapes and damping ratios often remain weakly affected (see e.g. Azzara et al. (2018)). Let us denote the time series of n_f identified resonant frequencies collected in an observation matrix $\mathbf{Y} = \left[\mathbf{y}_1, \ldots, \mathbf{y}_f\right] \in \mathbb{R}^{N \times n_f}$ containing N observations. In this light, data normalization constitutes the process of subtracting the reversible variability in the selected features in $\mathbf{Y}$ induced by benign EOC. This can be achieved by training a certain statistical model over a set of t_p samples from $\mathbf{Y}$ defining a baseline in-control population, $\mathbf{Y}_{tp} \in \mathbb{R}^{t_p \times n_f}$, often referred to as the *training period* (García-Macías and Ubertini (2022a)). This baseline dataset must represent the healthy condition of the structure under all possible EOC, being a one-year period often adopted. Among the wide variety of data normalization techniques available in the literature, Multiple Linear Regression (MLR) models represent a simple but powerful approach (García-Macías and Ubertini (2022b)). MLR models exploit linear correlations between the selected features in $\mathbf{Y}$ (estimators) and a set of p independent exploratory variables (predictors or independent variables), which are typically taken from monitoring data of EOC (e.g. temperature, humidity). The predictions by MLR $\hat{\mathbf{Y}}$ of the observation matrix $\mathbf{Y}$ are obtained as:

$$\hat{\mathbf{Y}} = \overline{\mathbf{P}}\,\overline{\boldsymbol{\beta}} = \left[\mathbf{1}_{N\times 1}, \mathbf{P}\right]\begin{bmatrix}\boldsymbol{\beta}_0^{\mathrm{T}} \\ \boldsymbol{\beta}\end{bmatrix}, \tag{12}$$

where $\mathbf{1}_{N\times 1}$ is a column vector of ones and $\mathbf{P} = \left[\mathbf{p}_1, \ldots, \mathbf{p}_p\right] \in \mathbb{R}^{N\times p}$ is an observation matrix with columns containing the time series of the p selected predictors. Term

$\boldsymbol{\beta}_0 \in \mathbb{R}^{n_f}$ is a vector of intercept terms and $\boldsymbol{\beta} \in \mathbb{R}^{p \times n_f}$ is a matrix of linear regression coefficients. Assuming normally distributed errors between the estimators and the predictions by the MLR model over the training period, the least squares estimate of the coefficients matrix reads:

$$\overline{\boldsymbol{\beta}} = \left(\overline{\mathbf{P}}_{tp}^{\mathrm{T}} \overline{\mathbf{P}}_{tp}\right)^{-1} \overline{\mathbf{P}}_{tp}^{\mathrm{T}} \mathbf{Y}_{tp}, \tag{13}$$

where subscript "*tp*" has been included to explicitly state that the MLR model is trained considering the set of predictors and estimators within the training period. Once constructed, the predictions of the MLR model $\hat{\mathbf{Y}}$ from Eq. (13) can be used to remove the variance due to EOC from $\mathbf{Y}$ through the so-called residual error matrix $\mathbf{E} \in \mathbb{R}^{N \times n_f}$, that is:

$$\mathbf{E} = \mathbf{Y} - \hat{\mathbf{Y}}. \tag{14}$$

When the system remains healthy, matrix $\hat{\mathbf{Y}}$ reproduces the part of the variance driven by EOC, while $\mathbf{E}$ only contains the residual variance stemming from modelling errors. Conversely, if a certain damage develops, matrix $\hat{\mathbf{Y}}$ remains unaltered while matrix $\mathbf{E}$ concentrates the damage-induced variance, being thus apt for damage identification.

5. Kriging meta-modelling

The construction of a SM generally comprises four consecutive steps as sketched in Fig. 4, including: (i) Selection of design variables; (ii) Sampling of the design space, (iii) Generation of the training population, and (iv) Construction of the SM. The definition of the design space consists in selecting all those parameters and their variation ranges required to parametrize the original FEM. Let us consider m design variables $x_i \in \mathbb{R}, i = 1, \ldots, m$ allowed to vary only within a certain physically meaningful range $[a_i, b_i]$. Accordingly, the vector of design variables $\mathbf{x} = [x_1, \ldots, x_m]^{\mathrm{T}}$ spans the m-dimensional design space $\mathbb{D} = \{\mathbf{x} \in \mathbb{R}^m : a_i \leq x_i \leq b_i\}$. As anticipated in Section 3, the selected model parameters must reproduce the effects of potential damage upon the investigated response y of the structure. In this light, a SM provides a computationally efficient functional mapping between the selected damage-sensitive parameters $\mathbf{x}$ and the response $y \in \mathbb{R}$ predicted by the FEM of the structure. In the case of non-intrusive SMs, it is necessary to assemble a training population of N_s individuals mapping the output y and the design space $\mathbb{D}$, also referred to as the experimental design (ED). This is accomplished by drawing a set of samples uniformly over the input design space $\mathbb{D}$ and building a matrix of design sites $\mathbf{X} = [\mathbf{x}^1, \ldots, \mathbf{x}^{N_s}] \in \mathbb{R}^{(m \times N_s)}$. Then, the corresponding outputs y^i are obtained by direct Monte Carlo simulations (MCS) using the main FEM and collected in an observation vector $\mathbf{Y} = \left[y^1, \ldots, y^{N_s}\right]^{\mathrm{T}}$. In this work, the elastic moduli of certain regions of the FEM (referred to as macro-elements hereafter) are defined as damage-sensitive design variables, whilst the modal properties extracted from a linear modal analysis of the FEM are assumed as outputs. Therefore, different SMs must be constructed for each natural frequency and modal amplitude of all the vibration modes involved in the analysis. Specifically, if l modes of vibration are selected and n_{DOF} degrees of freedom are used to characterize the mode shapes, a total of $l\,(1+n_{DOF})$ SMs must be constructed.

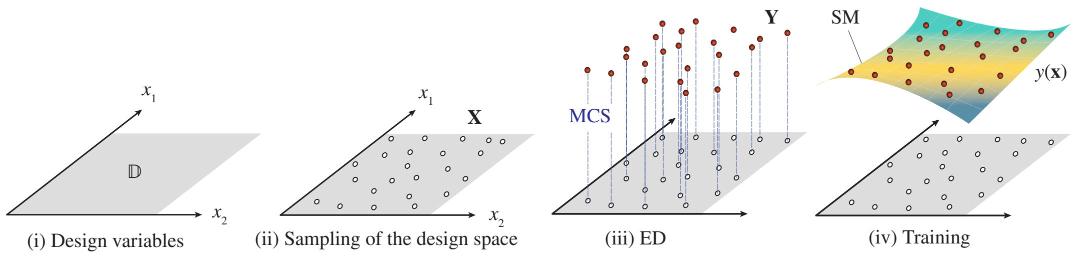

Figure 4. Schematic representation of the construction of a non-intrusive SM.

Among the wide variety of non-intrusive SMs available in the literature, the Kriging model is selected in this work owing to its high flexibility for adaptation to a wide variety of problems (Kleijnen (2009)). The Kriging interpolator conceives the function of interest $y(\mathbf{x})$ as the sum of a linear regression term $y_r\,(\mathbf{x})$ and a zero-mean stochastic process $\mathcal{Z}\,(\mathbf{x})$ as follows (Kleijnen (2017)):

$$y\,(\mathbf{x}) = y_r\,(\mathbf{x}) + \mathcal{Z}\,(\mathbf{x})\,. \tag{15}$$

It can be understood that $y_r\,(\mathbf{x})$ globally approximates the design space, whilst $\mathcal{Z}\,(\mathbf{x})$ introduces localized deviations. The regression function $y_r(\mathbf{x})$ depends upon p regression parameters $\boldsymbol{\kappa} = [\kappa_1, \ldots, \kappa_p]^{\mathrm{T}}$ and certain user-defined regression functions $f(\mathbf{x}) = [f_1(\mathbf{x}), \ldots, f_p(\mathbf{x})]^{\mathrm{T}}$ with $f_i : \mathbb{R}^m \to \mathbb{R}$ as (Stein (1999)):

$$y_r(\mathbf{x}) = f(\mathbf{x})^{\mathrm{T}}\boldsymbol{\kappa}. \tag{16}$$

The stochastic process $\mathcal{Z}\,(\mathbf{x})$ is determined by its covariance function $\mathrm{Cov}\,[\mathcal{Z}(\mathbf{x}_i)\mathcal{Z}(\mathbf{x}_j)]$ between any two arbitrary data points $\mathbf{x}_i$ and $\mathbf{x}_j$:

$$\mathrm{Cov}\,[\mathcal{Z}(\mathbf{x}_i)\mathcal{Z}(\mathbf{x}_j)] = \sigma^2 r\,(\mathbf{x}_i, \mathbf{x}_j, \boldsymbol{\theta})\,, \tag{17}$$

where σ^2 stands for the variance of $\mathcal{Z}\,(\mathbf{x})$, and $r\,(\mathbf{x}_i, \mathbf{x}_j, \boldsymbol{\theta})$ is a given spatial correlation function dependent on $\boldsymbol{\theta}$ parameters. On this basis, the Kriging predictions $\widehat{y}\,(\mathbf{x})$ of the response $y\,(\mathbf{x})$ at an arbitrary design site $\mathbf{x}$ are defined as:

$$\widehat{y}(\mathbf{x}) = f(\mathbf{x})^{\mathrm{T}}\boldsymbol{\kappa} + r(\mathbf{x})^{\mathrm{T}}\mathbf{R}^{-1}\left[\mathbf{Y} - f(\mathbf{x})^{\mathrm{T}}\boldsymbol{\kappa}\right], \tag{18}$$

where $r(\mathbf{x})$ is a vector containing the correlations between the design sites and $\mathbf{x}$, that is:

$$r(\mathbf{x})^{\mathrm{T}} = \left[r\,(\boldsymbol{\theta}, \mathbf{x}_1, \mathbf{x})\,, \ldots, r\,(\boldsymbol{\theta}, \mathbf{x}_{N_s}, \mathbf{x})\right]^{\mathrm{T}}, \tag{19}$$

and $\mathbf{R}$ is a $N_s \times N_s$ positive definite matrix with components $R_{ij} = r(\mathbf{x}_i, \mathbf{x}_j, \boldsymbol{\theta})$.

From Eq. (18), it is noted that, once the regression model and the correlation function are chosen, the Kriging interpolator is determined by the regression parameters $\boldsymbol{\kappa}$ and the correlation parameters $\boldsymbol{\theta}$. In this work, second-order polynomial regression functions are used to define the trend term, while Gaussian correlation functions are chosen as (Sacks et al. (1989)):

$$r(\mathbf{x}_i, \mathbf{x}_j, \boldsymbol{\theta}) = \prod_{k=1}^{m} \exp\left[-\theta_k \left(x_i^{(k)} - x_j^{(k)}\right)^2\right]. \tag{20}$$

Correlation parameters θ_k in Eq. (20) determine the shape of the correlation function, which may be anisotropic along the dimensions of $\mathbf{x}$. Nevertheless, in this work, correlations are assumed isotropic for the sake of simplicity, that is $\theta_k = \theta \quad \forall\, 1 \leq k \leq m$. Given the values of the correlation parameters $\boldsymbol{\theta}$, the trend coefficients $\boldsymbol{\kappa}(\boldsymbol{\theta})$ and the variance $\sigma^2(\boldsymbol{\theta})$ may be computed using the empirical best linear unbiased estimator (BLUE) as closed-form functions of $\boldsymbol{\theta}$ (refer to Kleijnen (2017); Stein (1999) for further details). Instead, the estimation of the correlation parameters $\boldsymbol{\theta}$ typically requires to solve a non-linear optimization problem, being the maximum-likelihood-estimator one of the most common approaches.

In this work, the construction of the SMs has been carried out through a set of in-house Python scripts. Specifically, the input samples of the ED in $\mathbf{X}$ are drawn by the quasi-random sequence of Sobol using the SciPy toolbox. Then, the observation vectors $\mathbf{Y}$ are extracted by MCS of the FEM of the Muhammad Tower developed in ABAQUS environment (Abaqus (2009)) as described hereafter in Section 6.2. To do so, a second Python script has been designed to modify the input ABAQUS file according to the samples in $\mathbf{X}$, launch linear modal analysis in ABAQUS, and read the resulting modal properties through text files. This script is launched iteratively for all the samples in $\mathbf{X}$ until completing the observation vectors $\mathbf{Y}$. Finally, the Kriging SMs are trained in a third Python script containing the previous formulation. In particular, the maximum-likelihood-estimator of the correlation parameters $\boldsymbol{\theta}$ is solved using the iterative pattern search optimization algorithm proposed by Lophaven et al. (2002) as implemented in the DACE toolbox.

6. Numerical results and discussion

This section reports the application of the proposed meta-model assisted St-Id approach previously introduced in Section 3 to the Muhammad Tower from January until March 2022. In particular, the numerical results and discussion are organised as follows. Section 6.1 presents the continuous dynamic identification of the tower and the analysis of environmental effects. Sections 6.2 and 6.3 report the construction the 3D FEM of the tower and the corresponding SM, respectively. Finally, Section 6.4 concerns the implementation of the proposed meta-model assisted St-Id of the Muhammad Tower and validation through several synthetic damage scenarios.

6.1. *Modal identification of the Muhammad Tower*

The dynamic identification approach in Section 4 has been implemented in an in-house software suite called MOVA/MOSS (García-Macías and Ubertini (2020)) dedicated to long-term SHM. The software code contains all the necessary tools for unsupervised damage detection, including (i) signal processing, (ii) automated OMA, (iii) modal tracking, (iv) data normalization, and (v) novelty analysis. All the 30 min-long acceleration records have been processed following a filtering sequence comprising: (i) elimination of linear trends, (ii) removal of anomalous spikes through Hanning window filtering, and (iii) second order high-pass Butterworth filter with a cut-off frequency of 2 Hz. Once cleansed, the acceleration time signals are used to extract the modal signatures of the tower following the automated Cov-SSI procedure previously reported in Section 4.1. To do so, the time-lag parameter j_b has been assumed as 193 (corresponding to a time lag of 3.2 s), and the system matrices and the corresponding modal features have been estimated considering model orders varying from 20 to 120 with steps of 2. For the identification of stable poles, the maximum allowable damping ratio ζ_{max} and the MPC and MPD limit values have been set to 10%, 80%, and 50%, respectively. The modal tolerances in the SC have been defined as $\Delta f \leq 1\%$, $\Delta\xi \leq 3\%$, and $MAC \geq 0.99$. After the application of the SC, the weighing factor η in Eq. (11) to perform the cluster assignments has been set to 0 (distance between the surviving stable poles and the modal clusters defined only in terms of resonant frequencies). Finally, a minimum size of 3% of the number of stable poles after the application of SC has been defined as a reasonable size to consider a cluster as a physical mode.

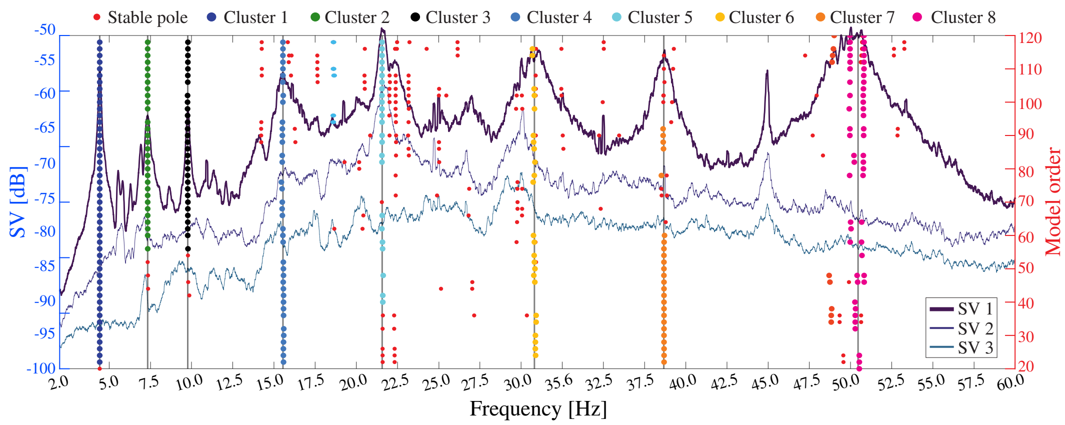

Figure 5. Stabilization diagram obtained by Cov-SSI of the Muhammad Tower (January 10$^{\text{th}}$ 2022 10:00 a.m.).

Figure 5 furnishes the stabilization diagram obtained by Cov-SSI of the first 30 min-long records acquired by the SHM system on January 10$^{\text{th}}$ 2022 at 10:00 a.m. The automated OMA procedure is applied to the stable poles depicted in Fig 5 in the frequency range between 0 and 60 Hz, leading to a total of 8 clusters with modal properties reported in Table 1. In the frequency broadband up to 10 Hz, three clear columns of stable poles are found at frequencies coincident with three evident resonant peaks in the first singular value (SV) of the spectral matrix. After inspection of the modal displacements shown in Fig. 6, these modes can be readily interpreted as global modes of vibration of the tower. Specifically, modes Fy and Fx are first-order bending modes along the N-S and W-E directions of the tower, respectively, while Tz is the first torsional mode of the tower. The remaining clusters in Fig 5 are also coincident with clear peaks in the first SV of the spectral matrix. Nevertheless, the inspection of their modal displacements did not reveal any global motion of the tower. These modes, labelled with L1 to L5, are conceivably ascribed to local modes of the battlements in the terrace of the tower. The local nature of high-order modes above 10 Hz was also confirmed by the FEM of the tower reported hereafter in Section 6.2. Nonetheless, it would be necessary to incorporate additional local sensors to confirm whether modes L1 to L5 actually correspond to local movements of the abutments. Note that the modal complexity of all the identified clusters is very low, with MPC values very close to 100%. This circumstance supports the consideration of all the identified clusters as physical modes.

Table 1. Experimentally identified modal signatures of the Muhammad Tower on January 10th 2022 10:00 a.m. and all throughout the monitoring period.

		January 10th 2022 10:00 a.m.			Continuous monitoring		
Mode No.	Label	Frequency [Hz]	Damping ratio [%]	MPC [%]	Mean Freq. [Hz]	Mean Damp. [%]	SR [%]
1	Fy	4.43	4.22	100.0	4.44 (±4.07%)	4.49 (±31.63%)	99.0
2	Fx	7.34	4.51	99.4	7.38 (±4.42%)	4.39 (±47.46%)	87.0
3	Tz	9.78	2.29	99.9	9.95 (±6.19%)	2.46 (±92.11%)	67.5
4	L1	15.56	3.64	99.8	16.50 (±13.97%)	2.17 (±128.00%)	45.6
5	L2	21.58	1.52	99.5	21.02 (±21.12%)	1.49 (±93.21%)	59.5
6	L3	22.41	1.79	99.5	-	-	-
7	L4	38.68	1.38	99.9	38.79 (±23.77%)	1.52 (±144.83%)	44.9
8	L5	50.47	1.27	99.7	51.40 (±23.41%)	1.61 (±163.08%)	72.4

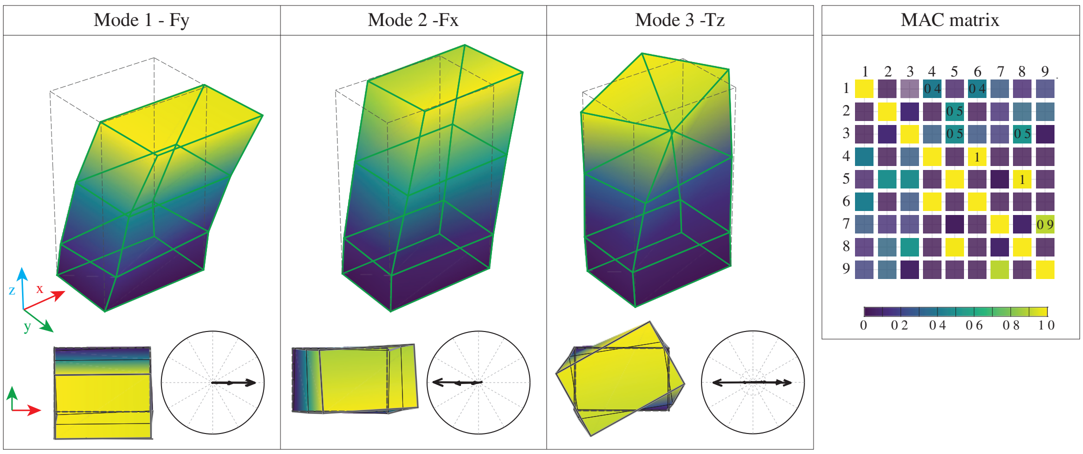

Figure 6. Experimentally identified global mode shapes of the Muhammad Tower on January 10th 2022 10:00 a.m.

The identification results obtained for the first acceleration record were used to define the baseline modal features of the tower to be tracked all throughout the monitoring period from January 10th until March 31st 2022 (3233 acceleration records). To avoid misclassification, the modal tracking is only conducted for sets of poles abiding with certain user-defined tolerances with respect to the reference modes. In particular, every time a new identification is performed, only the modal clusters that are proximate enough to any of the reference modes in terms of frequency and mode shape are kept in the modal tracking. In this case, maximum relative differences in frequency

$\Delta f \leq 5\%$ and MAC values $MAC \geq 0.85$ have been set for Modes 1 to 3, while frequency differences of $\Delta f \leq 15\%$ and MAC values $MAC \geq 0.75$ have been selected for the remaining modes. At every step of the tracking procedure, all the poles complying with these tolerances are assigned to the reference mode with the lowest distance metric from Eq. (11) with $\eta = 0.5$. On this basis, the time series of identified resonant frequencies are reported in Fig. 7 along with some statistical descriptors in Table 1. All the reference modes were tracked with a success ratio (SR) above 40% except for Mode L3, which could not be consistently identified and thus omitted herein. Note that the first three modes corresponding to global motions of the tower are consistently identified all throughout the monitoring period with an average SR of 82.5%. Conversely, the SRs in the identification of the high-order modes are considerably lower, which may be ascribed to the absence of accelerometers monitoring the local movements of the battlements. Also, the excitation level of the tower is considerably low, with mean accelerations of 0.15 cm/s^2. Given the poor identification of the local modes and their potentially limited sensitivity to identify the appearance of damage affecting the main body of the tower, only the time series of the resonant frequencies of Modes 1 to 3 are used hereafter. It is also noticeable in the detailed view in the bottom part of Fig. 7 that considerable oscillations indicating the presence of strong environmental effects are found in the global modes of the tower, particularly in Mode 2. Finally, it can be also observed that there are times at which the monitoring system was interrupted due to electrical supply shortage (mid-January to mid-February, and twice in March).

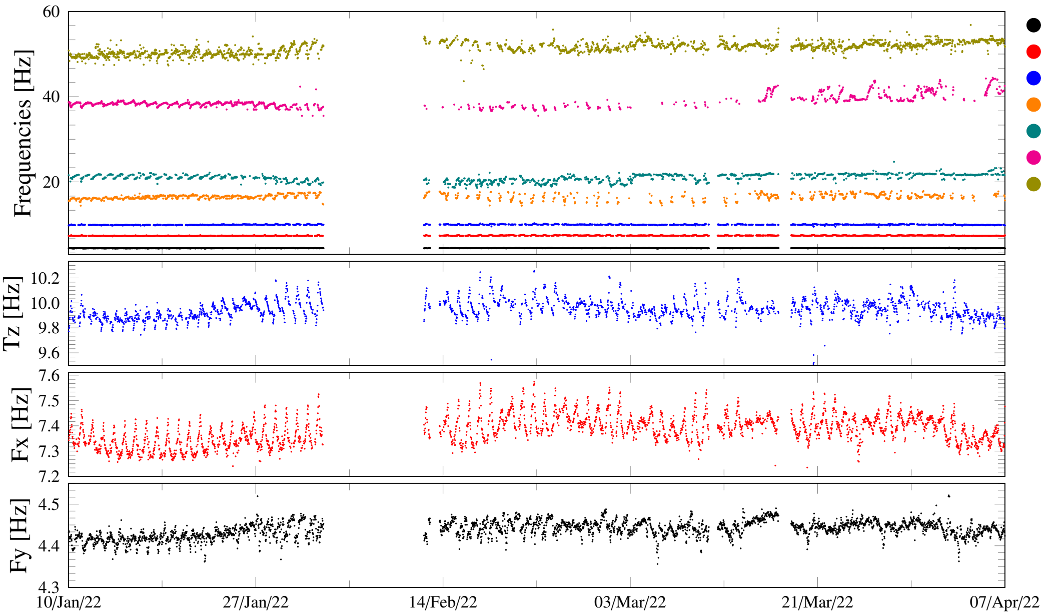

Figure 7. Tracking of the resonant frequencies of the Muhammad Tower from January 10th until March 31st 2022.

In order to ascertain the influence of EOC upon the identified modal signatures, correlation analyses with the environmental factors assessed by the Granada-Albayzín meteorological station were conducted as reported in Fig. 8. In particular, only noticeable correlations were observed between the identified resonant frequencies and air temperature (AT), humidity (H), and atmospheric pressure (AP) as reported in Figs. 8 (b,c,d), (e,f,g), and (h,i,j), respectively. The time series of the resonant frequency of Mode 2 (the mode in which the largest correlations have been found), temperature, humidity and air pressure are furnished in Fig. 8 (a). It is noted in this figure that the daily oscillations in the resonant frequency of Mode 2 (Fx) are particularly well correlated with temperature and humidity, exhibiting certain in-phase and opposite-phase trends, respectively. This circumstance agrees with the appearance of positive and negative correlations with air temperature ($R^2 = 0.69$) and relative humidity ($R^2 = 0.16$) as shown in Figs. 8 (c) and (f), respectively. This leads to increases in the resonant frequency during day-times and decreases during night-times (Fig. 8 (a)). Instead, note that the fundamental frequency Fy shows almost no correlation with temperature ($R^2 = 0.00$), humidity ($R^2 = 0.00$) nor air pressure ($R^2 = 0.04$) (Figs. 8 (b, e, h)). Finally, only low to moderate correlations are found for Mode 3 (Tz) (Figs. 8 (d, g, j)), with coefficients of determination of $R^2 = 0.25$ and $R^2 = 0.10$ with respect to air temperature and relative humidity, respectively. Note that bending motions concentrate in this mode along the N-S direction, where the walls of the Alhambra offer limited stiffness constraint. Conversely, Modes 2 and 3 do activate the longitudinal and bending stiffness about the axis of maximum inertia of the walls. This may indicate the walls of the fortress are particularly affected by EOC, which may explain the larger sensitivity of Modes Fx and Tz to EOC (Figs. 8 (c, d, f, g, i, j)). Indeed, only some weak correlation is observed between Mode Fy and air pressure ($R^2 = 0.08$), which may indicate wind actions might drive some of the observed fluctuations. Unfortunately, no reliable wind speed measurements could be obtained from the meteorological station due to malfunctioning of the anemometer, so further future investigations should address this aspect.

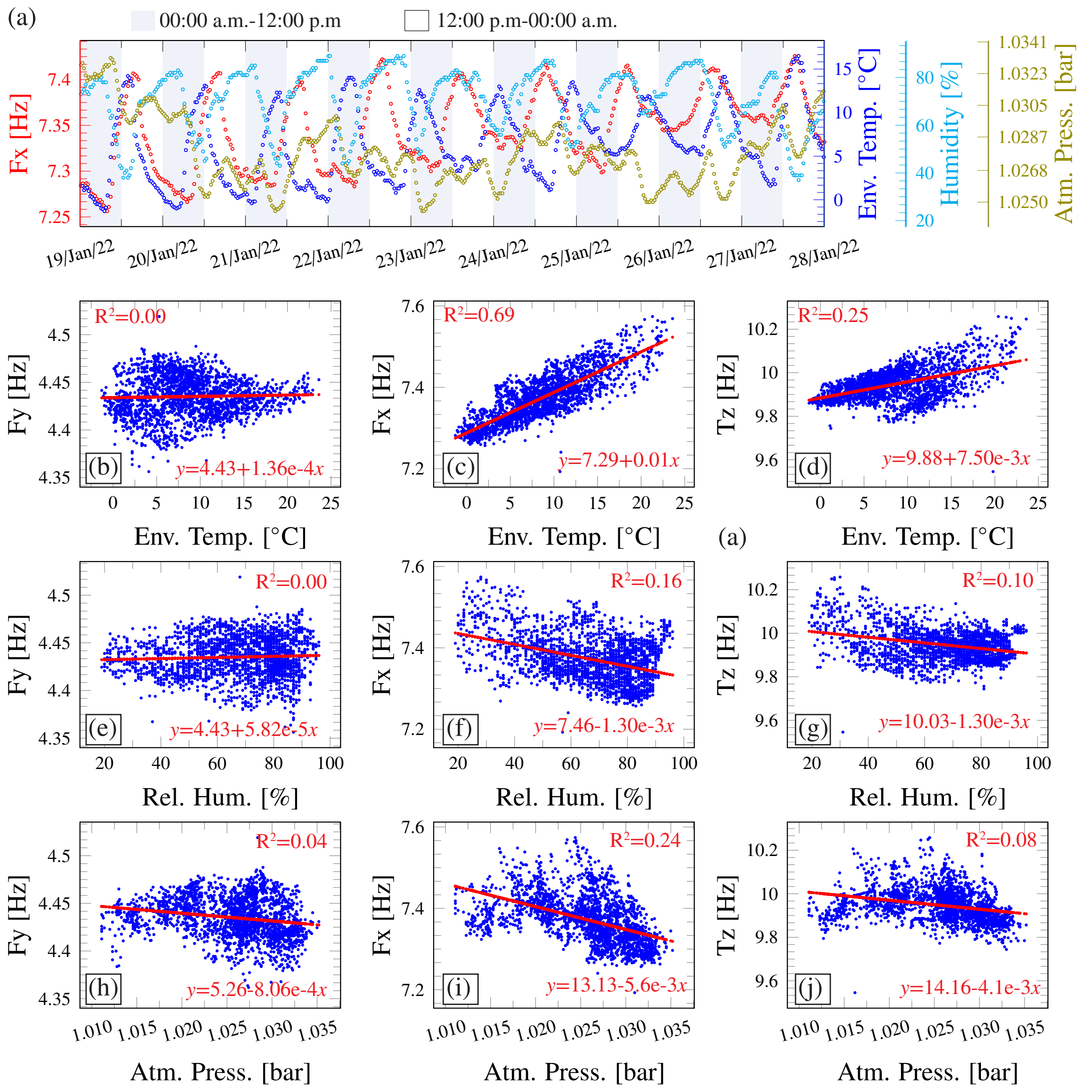

Figure 8. Time series of Mode 2 (Fx) and environmental data (January 19$^{\text{th}}$ until January 28$^{\text{th}}$ 2020) (a). Correlation analysis of the first three resonant frequencies of the Muhammad Tower, Mode 1 (Fy) (b,e,h), 2 (Fx) (c,f,i), and 3 (Tz) (d,g,j).

In view of the previous correlation analyses, the MLR model previously overviewed in Section 4.2 has been adopted to minimize the presence of EOC. Given the limited amount of monitoring data, the training period has been defined from January 10$^{\text{th}}$ until March 8$^{\text{th}}$ 2022 (2200 data points). Missing data in the time series of resonant frequencies have been completed using an autoregressive model constructed in segments of 96 data points around the missing data (corresponding to 2 days of monitoring data) and model's order of 3. The best combination of predictors in the MLR model was found after some manual tuning, and includes AT, H, AT^2, H^2 as well as two derived quantities obtained as the moving averages of AT with time windows of 48 (1 day) and 1344 (1 month) data points. The comparison between the experimental data and the predictions by MLR is reported in Fig. 9 (a). The quality of pattern recognition models is usually assessed by the inspection of the statistical distributions of the residuals as those shown in Fig. 9 (b). In the case of ideal normalization, the residuals in the training period should only contain normally distributed errors stemming from limitations in the identification of the healthy database as well as marginal EOC effects. In this light, it is first noted that all the residuals exhibit almost zero mean values μ (maximum value of 2.0E-15 Hz for Mode 1). In addition, kurtorsis values (κ) of 4.7, 3.9 and 6.5 are obtained for Modes 1, 2 and 3, respectively. Considering that $\kappa = 3$ is the theoretical value for a perfect Gaussian distribution, these results demonstrate that the best residuals have been obtained for Mode 2, while the quality of residuals E_1 and E_3 is considerably lower. Similar conclusions can be visually observed in the time series of residuals in Fig. 9 (b). Note in this figure that, in agreement with the correlation analyses in Fig. 8, the best fitting was obtained for Mode 2. Instead, even though the MLR model can reproduce the incipient seasonal trend and part of the daily oscillations of Modes 1 and 3, considerably poorer fittings were obtained for these modes. The poor performance of MLR to normalize these modes is ascribed to limited correlations with the assessed environmental factors as previously reported in Fig. 8. Nonetheless, given that the maximum error in terms of dispersion is only σ=5.8E-2 Hz for Mode 3, the conducted statistical pattern recognition is considered adequate for the purpose of this work. Future developments of this study will include the deployment of new environmental sensors assessing the local temperature of the tower (indoor and outdoor) to analyse the potential existence of capacitance effects as commonly observed in massive structures (Zonno et al. (2019), García-Macías and Ubertini (2022b)), as well as an anemometer to estimate the influence of wind actions upon the variability of the resonant frequencies.

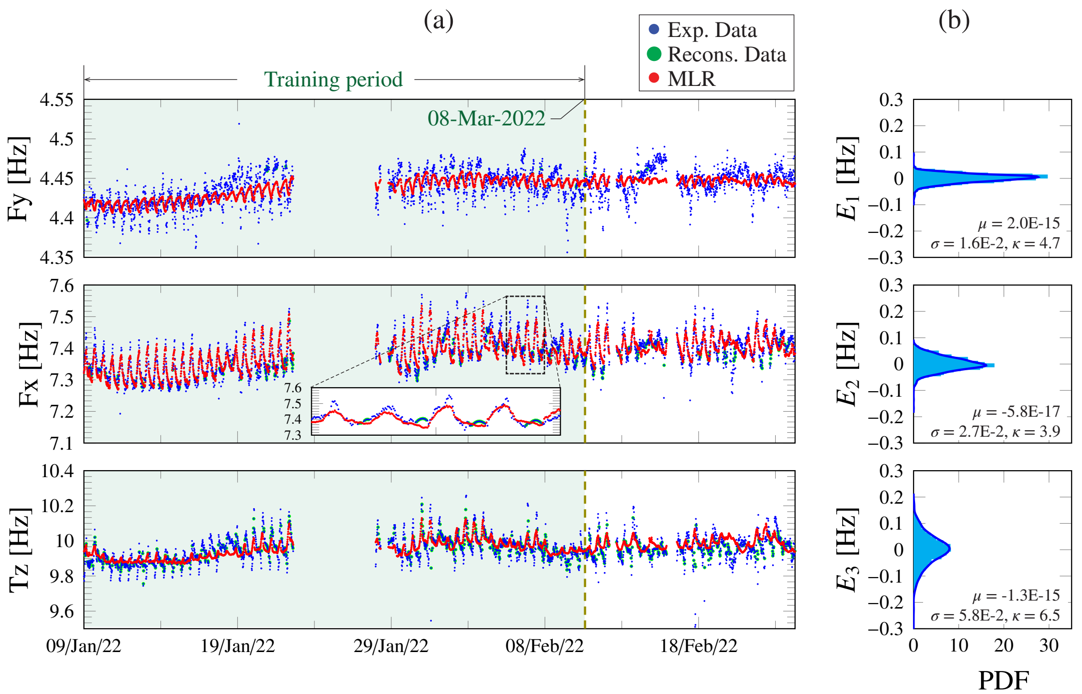

Figure 9. Minimization of EOC from the time series of the first three resonant frequencies of the Muhammad Tower by MLR (a), and probability distribution functions (PDFs) of the resulting residuals (b).

6.2. Finite element modelling and model calibration

With the aim of training the surrogate model with a realistic physics-based numerical model, a 3D FEM of the Muhammad Tower and the surrounding walls has been built using ABAQUS environment as shown in Fig. 10. The geometry of the model was constructed from information gained from available structural drawings and in-situ inspections. The walls, vaulted floors, openings, interior stairs and battlements are included in the model. In order to maintain a trade-off between computational burden and accuracy, only a small section of the walls of the Alhambra fortress (2.35 m thick and 7.29 high) is included in the model and rigidly connected to the main body of the tower. In particular, sensitivity analyses revealed that walls longer than 15 m produce no significant variations in the modal properties of the tower. Given the massive character of the structure, soil-structure interaction effects are disregarded and the base of the foundation and the adjacent walls are assumed fixed to the ground. Instead, to simulate the semi-buried condition of the south façade of the tower, sets of transverse and longitudinal spring elements were initially included in the model. Nevertheless, after some initial calibration by manual tuning, the stiffness of such springs resulted considerably large and hence fixed boundary conditions were eventually defined. The material model used for RE is assumed isotropic with elastic modulus 1.75 GPa, Poisson's ratio 0.3, and mass density 2.15 t/m^3. Note that, since one single homogenized material is considered for the whole model, the initial constitutive properties were selected between the values corresponding to brick masonry (1.44-1.45 t/m^3, and 1.6-3 GPa) and RE (2.1-2.3 t/m^3, and 1.2-6.3 GPa) from references Arto et al. (2021); Ávila et al. (2022b); González Limón and Casas Gómez (1997), the latter reporting the analysis of samples from the Tower of Comares, a proximate tower and with similar characteristics to the investigated one. The geometry has been meshed using 4-nodes C3D4 linear tetrahedral elements with mean size of about 50 cm after preliminary convergence analyses, which amounts to a total of 70898 nodes and 345642 elements.

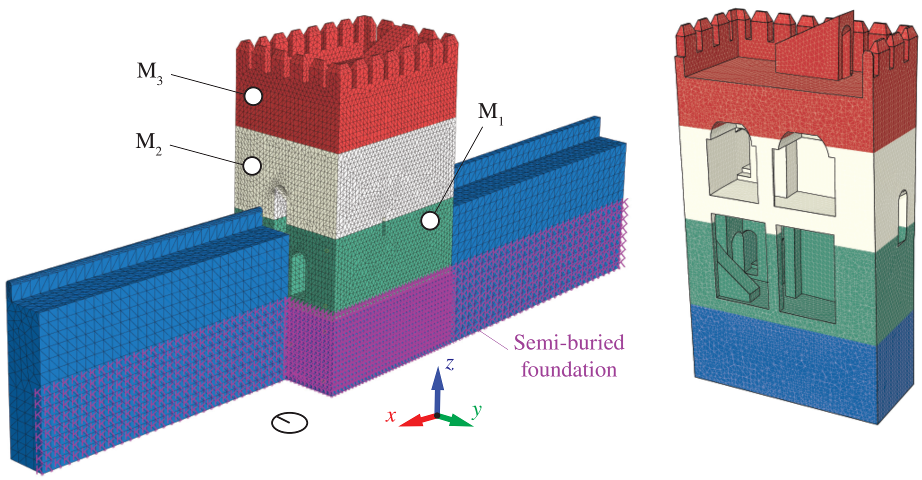

Figure 10. Partitioning of the FEM of the Muhammad Tower.

To minimize the uncertainty in the constitutive properties of the model, the elastic modulus and the mass density of the model have been initially calibrated through linear sensitivity analysis (Venanzi et al. (2020)):

$$\mathbf{X}_1 = \mathbf{X}_0 + \left(\mathbf{S}^{\mathrm{T}}\,\mathbf{S}\right)^{-1}\mathbf{S}^{\mathrm{T}}\left(\mathbf{f}_{\mathrm{exp}} - \mathbf{f}_{0,\mathrm{FEM}}\right), \tag{21}$$

where $\mathbf{X}_0$ and $\mathbf{X}_1$ denote the initial guess and the updated value of the model parameters, $\mathbf{f}_{\mathrm{exp}}$ and $\mathbf{f}_{0,\mathrm{FEM}}$ are vectors collecting the experimental (Table 1) and initially estimated natural frequencies, respectively, while $\mathbf{S}$ stands for the sensitivity matrix computed from the FEM by finite differences. As anticipated above, only the first three modes corresponding to global motions of the tower are considered in the calibration, while high-order local modes are disregarded in the calibration. The rationale for excluding those mode shapes is two-fold: (i) the sensors layout was not designed to provide an accurate representation of the local mode shapes, and (ii) the sensitivity of those modes to defects affecting the stiffness of the main body of the tower are conceivably minimum. The calibration resulted in a value of the Young's modulus of the tower of 1.97 GPa and a mass density of 2.42 t/m^3. Table 2 summarizes the comparison between the experimental modal signatures and those predicted by the tuned FEM, and the comparison of the numerical and experimental mode shapes is shown in Fig. 11. In general, very good agreements were found in terms of resonant frequencies with a mean error value of 1.28% and MAC coefficients close to 1.

Table 2. Comparison between experimental and numerical modal properties after FEM calibration. The experimental resonant frequencies have been obtained by automated Cov-SSI of the first 30 min of ambient vibrations of the Muhammad Tower recorded on January 10$^{\mathrm{th}}$ 2022 10:00 a.m.

Mode No.	Label	Experimental [Hz]	Numerical [Hz]	Error [%]	MAC
1	Fy	4.419	4.530	2.51	0.98
2	Fx	7.317	7.312	-0.07	0.94
3	Tz	9.788	9.666	-1.24	0.95

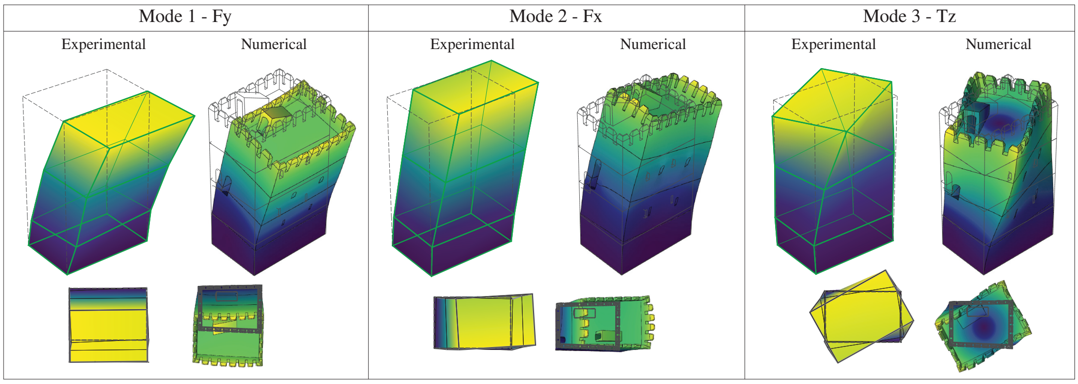

Figure 11. Comparison between experimental and numerical mode shapes of the Muhammad Tower.

It is important to remark that one linear modal analysis of the FEM of the Tower approximately takes 5 minutes in a standard PC (64-bit, 16.0 GB RAM, Intel(R) Core(TM) i7-8750H processor, 2.20 GHz CPU). Note that, since the optimization problem previously introduced in Section 3 typically requires an elevated number of model evaluations, such a computational burden impedes the direct implementation of the FEM for continuous SL damage identification. This circumstance justifies the construction of the proposed SM. To do so, a simple parametrization of the model has been defined by partitioning the tower into three macro-elements M_l (M_1 in $z \in [0.0, 7.8]$, M_2 in $z \in [7.8, 11.8]$, and M_3 in $z \in [11.8, 15.9]$) as shown in Fig. 10. The aim of such a partitioning is to provide a flexible parametrization capable of identifying a variety of earthquake-induced damage pathologies affecting the bending stiffness of the tower. In the subsequent analyses, the elastic moduli of the macro-elements are selected as damage-sensitive parameters for the Kriging SM. It is important to remark that different model parametrizations may be required depending on the target damage pathology to be assessed. Nonetheless, this would only represent a distinct definition of the design parameters $\mathbf{x}$, while the general methodology proposed in Section 3 would remain unaltered.

With the purpose of validating the proposed SM-based damage identification approach, different earthquake-induced damage scenarios have been simulated through a displacement-controlled pushover analysis. This consists in a non-linear static analysis where the tower is subjected to gravity loading and increasing lateral displacements along the NS direction following a parabolic profile. In order to reproduce the non-linear behaviour of RE, the CDP constitutive model (Abaqus (2009)) with cracking in tension and crushing in compression has been adopted. Given the lack of characterization tests of the RE of the tower, the non-linear mechanical properties assigned to the FEM have been estimated from the literature as shown in Table 3. For simplicity, and given that the interest is focused on the simulation of damage patterns affecting the dynamics of the tower, the walls of the fortress have been replaced by linear springs. The stiffness of these springs has been manually tuned until reproducing the same modal properties as the original FEM, achieving maximum differences in frequency below 5%. Figure 12 furnishes the monitored base shear force versus top displacement. In this light, ten different damage scenarios, labelled from DS1 to DS10, are defined as indicated in Fig. 12 (a). Samples of the damage patterns for DS1, DS4, DS6, DS8, DS9 and DS10 are represented in Fig. 12 (b) in terms of contour maps of the tensile damage parameter d_t. Note that d_t denotes the material degradation, and spans from 0 (undamaged material) to 1 (complete loss of strength). The main failure mechanism consists of a major horizontal crack originating from the door opening in the first level of the tower until crossing completely the north façade (DS1, DS2). Another major diagonal crack propagates upward from the door opening in the second level (DS1), although it does not cross the north façade until DS3. Some other secondary cracking patterns can be also observed as a result of stress concentrations in the remaining openings all throughout the tower. The structure loses completely its load bearing capacity when the main horizontal crack crosses entirely the cross-section of the tower for a maximum top displacement of 27.8 cm (DS10).

Table 3. Mechanical parameters utilized in the CDP model for RE (from Arto et al. (2021); Bui et al. (2020); García-Macías et al. (2021); GB 50010-2010 (2010); González Limón and Casas Gómez (1997)).

Elasto-plastic behaviour		**Tensile behaviour**		
K_c[a]	0.667	Tensile stress σ_t [kN/m^2]	Cracking strain $\tilde{\varepsilon}_t^{ck}$ [-]	Tensile damage d_t [-]
Eccentricity	0.10	300	0.00E-00	0.00
Viscosity parameter[b]	0.003	212	8.40E-04	0.29
Dilation angle [°]	21	153	1.67E-03	0.49
		90	3.36E-03	0.70
		62	5.04E-03	0.79
		48	6.71E-03	0.84
		32	9.23E-03	0.90

[a] K_c is the ratio of the second stress invariant on the tensile meridian.
[b] The viscosity parameter is used for the viscoplastic regularization of the constitutive equations.
* Compressive strength σ_c = 2450 kN/m^2.

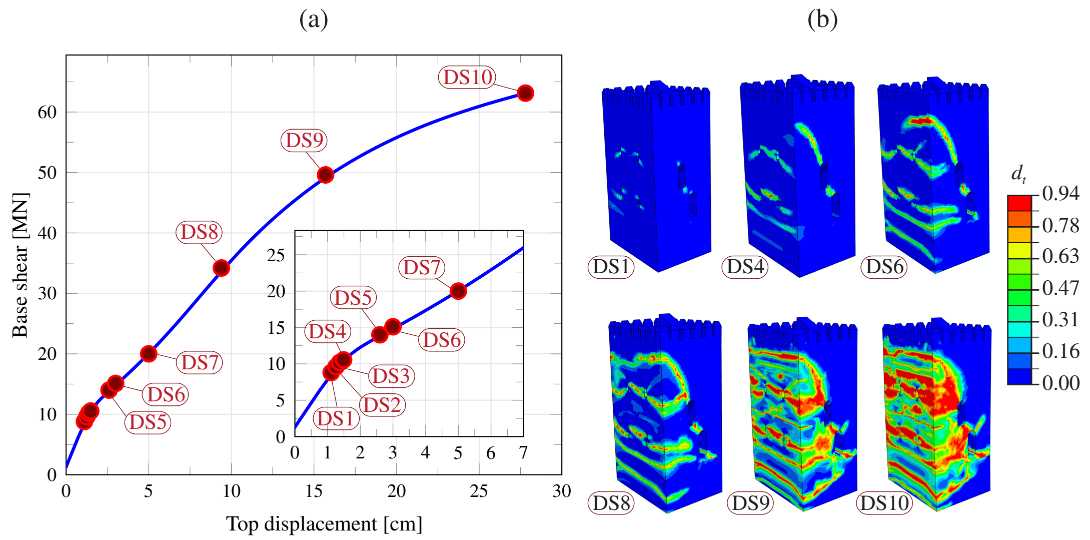

Figure 12. Base shear force versus top displacement curve obtained by displacement-controlled pushover analysis of the Muhammad Tower (a) and simulated crack patterns in the tower (b).

In order to include synthetic damage scenarios into the experimental time series of modal features previously reported in Section 6.2, every scenario in Fig. 12 (from DS1 to DS10) has been characterized through non-linear modal analysis. This consists in releasing the imposed lateral displacement in the model when the corresponding maximum displacement is achieved, followed by a modal analysis based on linear perturbation. The latter considers the tangent stiffness matrix of the FEM, which allows accounting for the damage-induced stiffness degradation on the modal properties of the tower (similar experiences on the combination of the CDP model and linear perturbation modal analysis can be found in the works by Hanif et al. (2016) and Scozzese et al. (2019)). This leads to the results reported in Fig. 13 where the frequency decays (a) and MAC values (b) of the first three modes of vibration are plotted against the top displacement. The frequency decays start to increase when the top displacement overpasses a value of about 1.25 cm (which roughly corresponds to a return period of 20 years according to the NCSE-02 Spanish Norm), that is when the main failure mechanism in the tower activates (drift ratios of 1.45‰ and 0.78‰ with respect to the height of the free-standing portion of the total height of the tower, respectively). Damage-induced effects primarily concentrate in terms of resonant frequencies, achieving maximum decays of up to about 14-18% for DS10, while only slight variations are observed in the mode shapes. Even though the pushover analysis is conducted along the N-S direction affecting Mode 1, frequency decays concentrate in Mode 2 as a result of larger stress concentrations in the E-W walls induced by the higher concentration of openings and the subsequent stiffness loss in this direction. From the experience of the authors, frequency decays around 1% are commonly detectable in heritage constructions by dynamic-based SHM. Therefore, only damage scenarios DS1 to DS7 are selected hereafter to appraise the effectiveness of the proposed SM-based St-Id for damage localization and quantification.

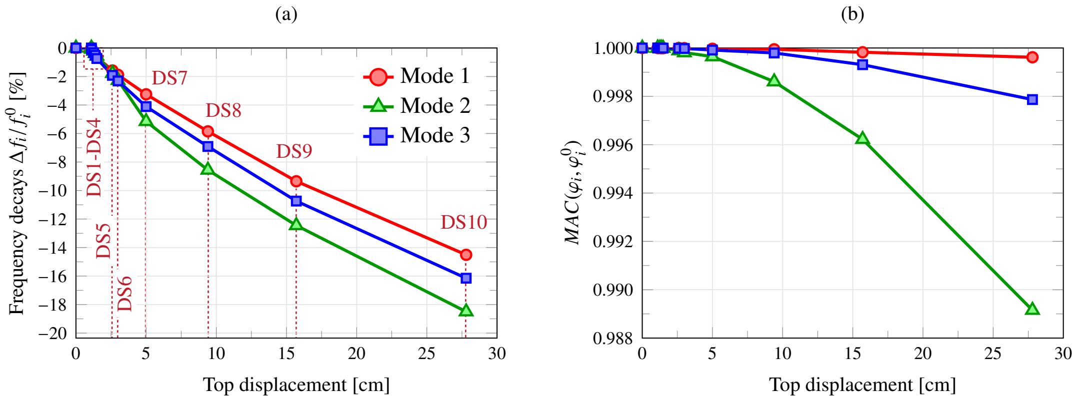

Figure 13. Frequency decays (a) and MAC values (b) of the first three modes of vibration obtained by the displacement-controlled pushover analysis of the FEM of the Muhammad Tower.

6.3. Construction of the SM

The accuracy of any SM is primarily determined by the quality in the sampling of the ED. The density of the training population is highly case-dependent, and it typically needs to be tailored according to the variability of the quantity of interest and the presence of non-smoothness and non-linearities. In general, the design space must be uniformly sampled to cover the whole domain of interest. Following the parametrization of the FEM into macro-elements from Fig. 10, the design variables have been defined as stiffness multipliers k_i, $i = 1, \ldots, 3$, affecting the elastic moduli of macro-elements M_i. The stiffness multipliers are assumed to be uniformly distributed within the variation domain $[0.7, 1.2]$. Note that such a variation range is considerably large, with 0.7 meaning a reduction of 30% of the elastic modulus of the affected macro-element. In this light, random samples have been drawn uniformly over $\mathbb{D} = \left\{\mathbf{k} \in \mathbb{R}^3 : 0.7 \leq k_i \leq 1.2\right\}$ using the quasi-random sequence of Sobol (Sobol (1967)). In order to select the size of the ED, a convergence analysis has been conducted considering different training populations with N_s=20, 40, 80, 120, and 160 individuals and a validation set (VS) of 200 samples as shown in Fig. 14 (a). For every population, the modal signatures corresponding to each individual are obtained by forward evaluation of the 3D FEM, being this step the most computationally intensive stage in the procedure. Since the first three modes of the tower have been considered in the analysis, a total of 27 SMs

(3 resonant frequencies plus 8×3 modal displacements) are built. Convergence is evaluated in terms of the statistical moments of the modal estimates in Fig. 14 (b), as well as some error metrics between the estimates of the SM and the FEM in Fig. 14 (c). In particular, the error in the prediction of the resonant frequencies is assessed through the root-mean-square-error (RMSE) and the coefficient of determination R^2. To appraise the quality in the estimation of the mode shapes, a metric $J_{(MAC,r)}$ accounting for the median of the $1 - MAC$ values between the r-th exact mode shape φ_r and the predictions by the SM $\hat{\varphi}_r$ in the VS is introduced as:

$$J_{MAC,r} = \mathrm{med}\left\{1 - MAC\left(\varphi_r, \hat{\varphi}_r\right)\right\}. \tag{22}$$

The analyses in Fig. 14 (b) show that the mean values of the resonant frequencies exhibit a slowly decreasing trend for increasing EDs (except for $N_s = 120$ that presents a local increase). In addition, the dispersion of the distributions in terms of statistical variance achieves convergence right after the population of 40 individuals. With respect to accuracy of the corresponding SMs in Fig. 14 (b), it is noted that the fitting errors decrease drastically at the population of 40 individuals, after which the accuracy stabilizes and only limited enhancements are obtained. In view of these results, a population of 160 individuals is selected to train the SMs as a conservatively accurate solution. The comparison between the predictions of the resulting SM and the forward FEM is shown in Fig. 15. The low scatter of the data points around the diagonal line corroborates that the SMs are formed with accuracy, with coefficients of determination R^2 very close to 1 and maximum root-mean-squared-errors (RMSE) of 3.8E-4 Hz. Note in Fig. 15 that very low $J_{(MAC,r)}$ values are obtained for all the considered mode shapes, which demonstrates the high accuracy of the SMs to reproduce the modal displacements. An essential aspect of the SM regards its computational cost. Note that the evaluation of the modal properties of the Muhammad Tower only requires 0.02 s, that is a reduction of 99.998% with respect to the forward model.

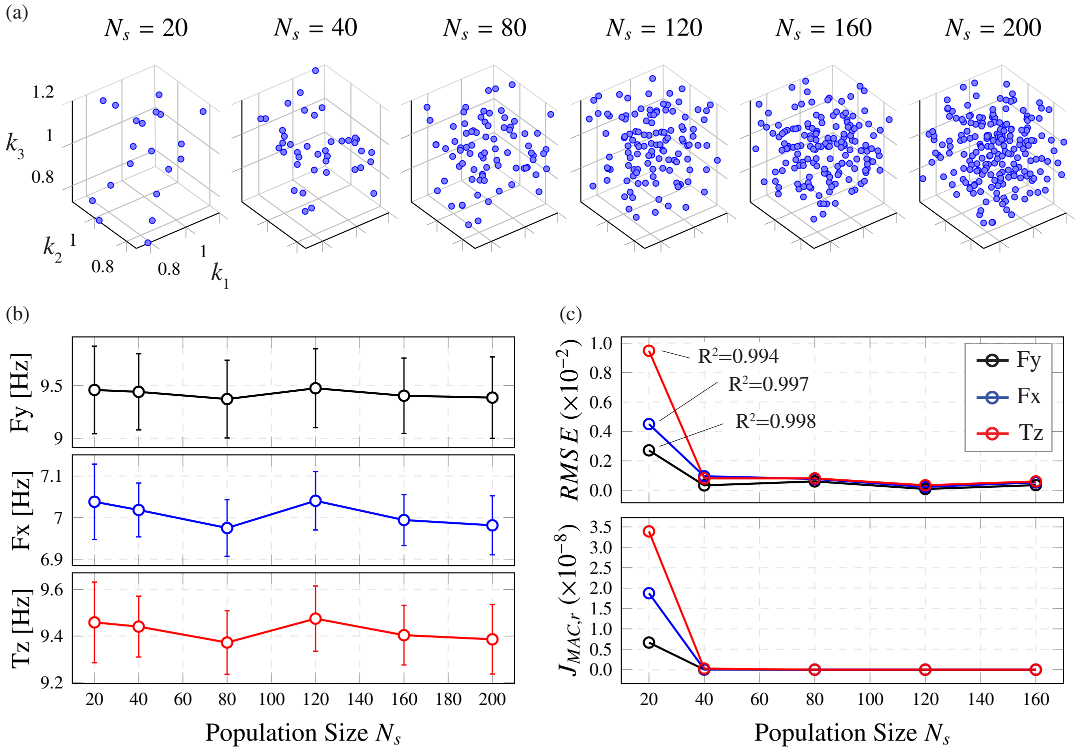

Figure 14. Training populations with increasing sizes obtained by Sobol sampling (a). Convergence analysis of the resonant frequencies of the Muhammad Tower (b), and the estimates of the Kriging SM for increasing population sizes (c). Error bars in (b) denote the variance in the distributions.

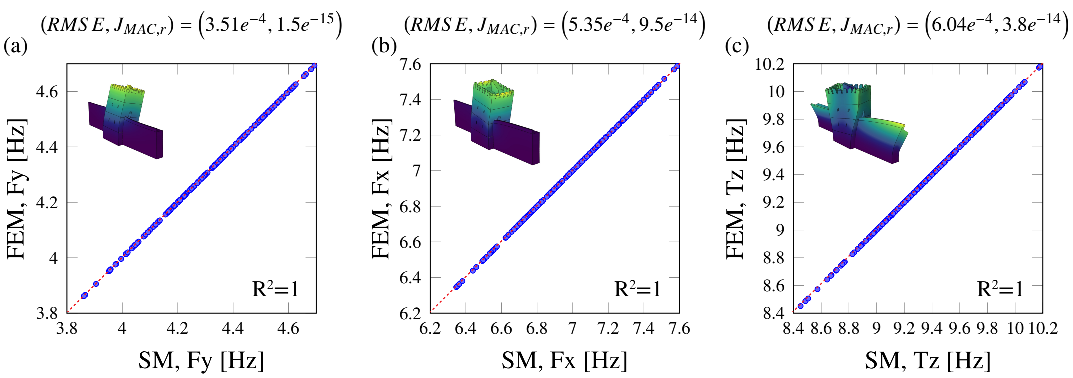

Figure 15. Scatter plot of the predictions by the Kriging SM (160 training samples) versus the forward evaluations of the 3D FEM of the Muhammad Tower: (a) Fy, (b) Fx, (c) Tz.

6.4. Continuous St-Id of the Muhammad Tower

This last section presents the results of the meta-model assisted St-Id approach previously introduced in Section 3 when applied sequentially to each set of identified modal data (30 min) over the testing period from January 10th until March 31st 2022. To this aim, the non-linear minimization problem in Eq. (3) is solved using a Particle Swarm optimization algorithm with 40 particles and error tolerance of 1E-5. In the regularization term $\mathcal{R}(\mathbf{x})$, a reference vector of design variables $\mathbf{k}^0 = [1, 1, 1]^{\mathrm{T}}$ is considered (i.e. $\mathbf{k}^0$ represents the situation when macro-elements M_i possess undamaged nominal Young's moduli). In addition, the variation range of the parameters is set to $0.7 \leq k_i \leq 1.2$ as specified in the training of the surrogate model. The weighting parameters $\eta_{(1,i)}$ and $\eta_{(2,i)}$ in the cost function in Eq. (3) have been defined after some manual tuning as $\eta_{(1,1)} = \eta_{(1,2)} = 1.0$, $\eta_{(1,3)} = 0.3$ and $\eta_{(2,1)} = \eta_{(2,2)} = \eta_{(2,3)} = 0.5$. Note that the weight given to the third resonant frequency (Tz) is lower than those assigned to the first two modes. Given the limitations of the MLR model to remove the effects of EOC from this frequency as previously reported in Fig. 9, the selection of this low value is intended to minimize the effects of residual variances on the subsequent St-Id.

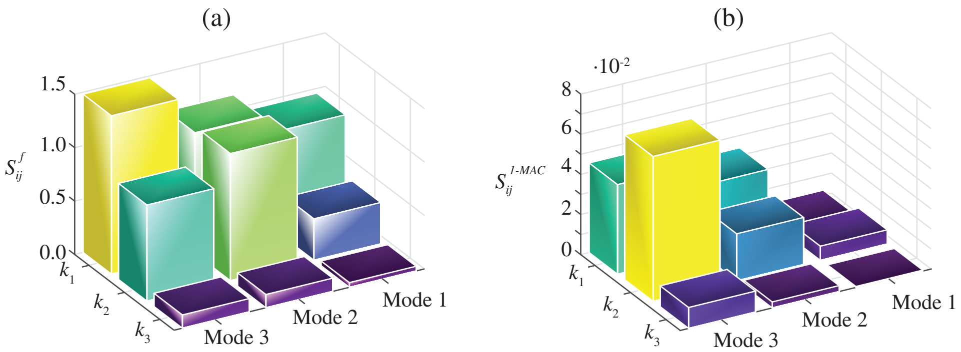

Figure 16. Model sensitivities of the 3 macro-elements of the 3D FEM of the Muhammad Tower in terms of resonant frequencies (a) and mode shapes (b).

For the definition of the trade-off parameters $\eta_{(3,i)}$, it is important to inspect the sensitivities of the model response with respect to variations in the design variables k_i. Figure 16 represents the sensitivity of the modal estimates in terms of resonant frequencies S_{ij}^{f} and $1 - MAC$ values S_{ij}^{1-MAC}, $i, j = 1, \ldots, 3$, computed using the 3D FEM and finite differences. While in classical model updating the parameters with the least sensitivities are typically excluded from the optimization or clustered together with other design parameters, such an approach would impede the localization of damage in certain regions of the structure. In this particular case study, the low sensitivity of the modal features of the tower to variations in k_3 considerably hinders the location of damage in M_3 (top macro-element). In this light, with the aim of accommodating the different sensitivities and as an attempt to maintain the damage localization capabilities in M_3, larger regularization parameters $\eta_{(3,i)}$ are assigned to the design variables with lower sensitivities. In particular, after some iterations by manual tuning, good results have been obtained when assuming $\eta_{(3,1)} = 0.30$, $\eta_{(3,2)} = 0.72$, $\eta_{(3,3)} = 1.2$.

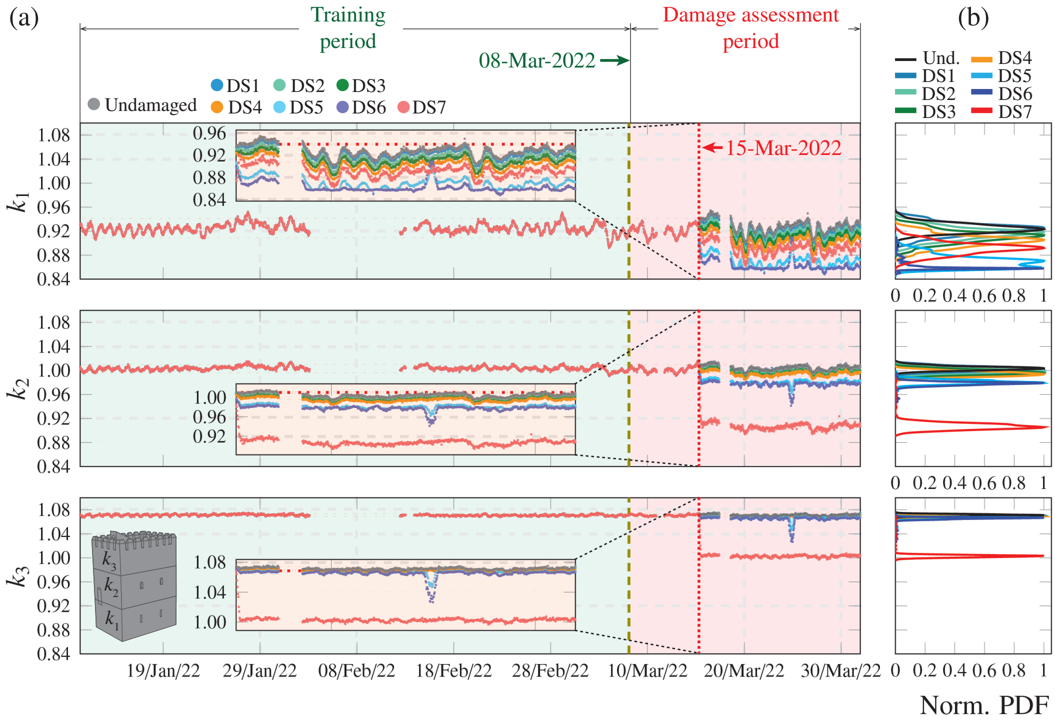

Figure 17. Time series of identified stiffness multipliers k_i of macro-elements M_i, $i = 1, \ldots, 3$, of the Muhammad Tower (a) and PDFs of data-points in the damaged period for synthetic damage scenarios DS1 to DS7 (b).

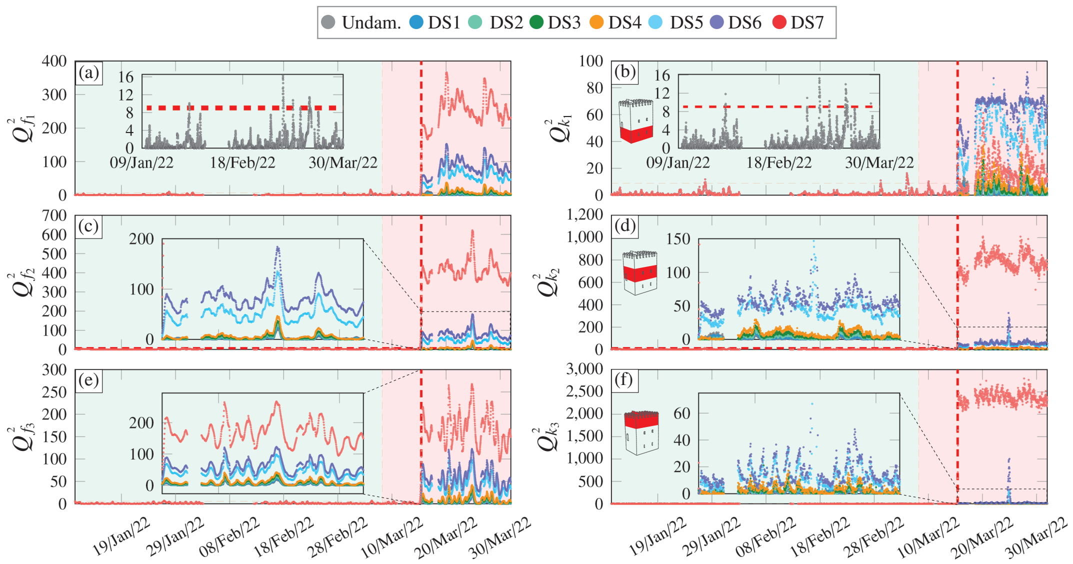

Figure 18. Mahalanobis distances with respect to the in-operation training period in terms of the first three fundamental frequencies of the Muhammad Tower (a,c,e) and the identified stiffness multipliers k_i (b,d,f) for synthetic damage scenarios DS1 to DS7. Red dashed lines stand for the 99% confidence level of the considered features empirically estimated for the training period.

The considered damage scenarios have been incorporated in the time series of modal features from March 15th 2022 (after the training period) by means of the frequency decays previously reported in Fig. 13 (a). Given the minimal impact of the considered damage scenarios upon the mode shapes of the tower, the time series of experimental modal displacements have been maintained unaffected. In this light, the outcomes of the continuous meta-model assisted St-Id are presented in Figs. 17 and 18. Figures 17 (a) and (b) depict the time series of identified stiffness multipliers k_i and the corresponding histograms after the application of damage, respectively. In addition, Fig. 18 presents the squared Mahalanobis distances with respect to the training period as a novelty analysis metric in terms of resonant frequencies and stiffness multipliers. It is clear in these figures that all the considered damage scenarios except for DS1 can be detected in the shape of sudden drops in the time series of k_i after the damage condition is imposed. Although some slight decreases are noticeable for DS1 in k_1 with respect to the undamaged condition (see the zoom insert in Fig. 17 (a)), the frequency decay associated with this damage scenario is lower than the residual variance in the normalized time series of resonant frequencies and, therefore, goes unnoticed. Instead, the damage-induced frequency decays of the remaining scenarios overpass the residual variances and, therefore, appear as clear anomalies in the time series of the stiffness parameters. Furthermore, these results evidence the localization and quantification ability of the proposed approach, allowing to effectively track the evolution of damage in the tower. Specifically, note in Fig. 17 that scenarios DS1 to DS4 primarily affect the stiffness of macro-element M_1 with increasing severities. Moreover, some slight decreases can be also observed in k_2, while almost no effects are noticeable in k_3. These results coincide with the damage patterns previously furnished in Fig. 12 (b), which reported the initiation and propagation of the major horizontal crack (affecting M_1) from DS1 until DS4. Afterwards, new diagonal cracks affecting macro-elements M_2 and M_3 originate, which agrees with the anomalies observed in Figs. 17 and 18 for DS5, DS6 and DS7. In particular, note that no significant degradation is found in k_3 until DS7, when the diagonal crack originating at the upper corner of the opening in the second floor crosses the North façade of the tower (see Fig. 12 (b)). Interestingly, it is noted in Fig. 17 (a) that the stiffness degradation for DS7 in k_1 decreases with respect to the values obtained for DS5 and DS6. This circumstance has no physical justification and evidences some limitations in the St-Id. On one hand, this may be due to the natural limitation of any model parametrization that does not explicitly represent the damage mechanism under analysis, as it is the case in these analyses since the model does not consider any particular parameter accounting for the specific crack pattern observed in Fig. 12 (b). On the other hand, despite the implementation of the regularization function $\mathcal{R}$, the circumstance that only three modes are consistently identified in the experimental campaign represents an observability limitation. These aspects certainly give origin to important sources of ill-conditioning, which may explain the aforementioned inconsistency in the damage identification. Nonetheless, given that DS7 represents an extremely severe damage condition, it can be concluded that the proposed meta-model assisted St-Id is proficient for damage identification of early-stage and moderate damage pathologies. It is noticeable in Fig. 18 that the damage-induced anomalies are more easily detectable in terms of stiffness multipliers, which furthers justify the use of the proposed methodology as a complementary approach to traditional OMA-based SHM. Finally, it is important to remark that the computational time to perform the St-Id is only around 7.4 s, which guarantees the compatibility of the proposed approach with long-term SHM applications.

Finally, a comprehensive damage index D_i is depicted in Fig. 19 to summarize the previous damage identification results. The damage index is simply defined as the relative variation of the medians of the time series of stiffness multipliers k_i in the damaged period with respect to the healthy baseline. It is noted in this figure that increasing damage indexes are obtained as the damage condition progresses, strengthening the discussion above on the ability of the proposed approach to localize and quantify damage. Moreover, these results highlight the impossibility of properly identifying DS1 and DS2 as a consequence of the afore-mentioned limitations in the statistical pattern recognition and the inverse model calibration, respectively.

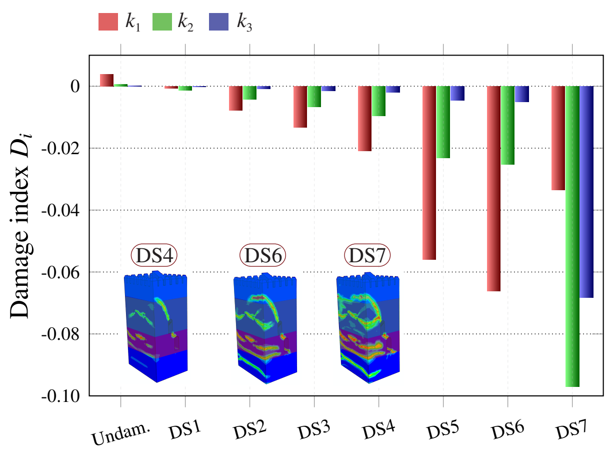

Figure 19. Damage indexes D_i in the three macro-elements M_i defined in the Muhammad Tower obtained for synthetic damage scenarios DS1 to DS7.

7. Concluding remarks

This work has presented the development of a meta-model assisted St-Id approach for online damage identification of a 13th century RE tower, the Muhammad Tower in the Alhambra (Granada, Spain). The developed meta-model has been fed with a continuous data-flow from an ambient vibration-based SHM system installed in the tower since January until March 2022. Through automated OMA, the modal signatures of the tower have been continuously extracted, and the presence of reversible oscillations induced by EOC has been minimised by means of statistical pattern recognition. Then, the normalized time series of modal signatures have been used to conduct St-Id and damage assessment. To this aim, a high-fidelity 3D FEM of the Tower has been developed and used to train a computationally light Kriging SM. Specifically, a simple parametrization of the tower into horizontal macro-elements has been designed as a flexible solution to identify earthquake-induced defects affecting the bending stiffness of the main body of the tower. It is important to strengthen that the model parametrization must be tailored according to the target damage pathology under investigation. Nevertheless, the presented methodology is general for any model parametrization, being only necessary to adapt the training phase of the Kriging SM. Numerical results and discussion have been reported on the characterization of environmental effects, quality assessment of the SM, and evaluation of damage identification capabilities by several synthetic damage scenarios obtained through non-linear simulations. Overall, the presented results and discussion have demonstrated the potential of the developed meta-model assisted St-Id for online damage identification, attaining computational times that are fully compatible with continuous SHM schemes. The key findings of this work can be summarised as:

- Three global modes have been consistently identified all throughout the monitoring period. In addition, up to 5 high-order modes have been also found in the frequency broadband up to 60 Hz, possibly related to local motions of the battlements of the tower.
- Clear correlations between air temperature and relative humidity have been found for two global modes involving the motion in the longitudinal and in-plane direction of the walls of the Alhambra fortress where the tower is inserted. Conversely, the fundamental mode activating the out-of-plane stiffness of the walls reveals almost no correlation with environmental data.
- Positive and negative correlations have been found between the resonant frequencies of the tower and environmental temperature and humidity, respectively. Such a positive correlation with temperature may be ascribed to thermal-induced closure of micro- and macro-cracks, while the negative correlation with relative humidity may indicated the presence of moisture-induced softening of the RE.
- The presented results have demonstrated the ability of the proposed meta-model assisted St-Id approach to identify damage (detection, localization and quantification) when the associated effects are larger than the residual variance in the normalized time series of modal signatures originated by limitations in the statistical pattern recognition.

Forthcoming works will include the local monitoring of the battlements with the aim of differentiating between local and global modes. Furthermore, the presented statistical pattern recognition approach will be used to evaluate the impact of structural interventions scheduled to retrofit the damaged battlements of the tower after the seismic swarm occurred from February until August 2021.

Acknowledgements

This work has been supported by the Secretaría General de Universidades, Investigación y Tecnología and by the Secretaría General de Vivienda de la Junta de Andalucía (Spain) through the research projects "Revalorización Estructural del Patrimonio Arquitectónico de Tapial en Andalucía" [Ref: A-TEP-182-UGR18] and "Metodología para el Análisis de la Integridad Estructural del Patrimonio Arquitectónico construido en tapial" [Ref: UGR.20-12], respectively. The collaboration of Prof. Nicolás Velilla from the Department of Mineralogy and Petrology from the University of Granada to access the environmental data of the Granada-Albayzín meteorological station is gratefully acknowledged. Finally, the support and information provided by Patronato de la Alhambra y el Generalife are also warmly acknowledged.

References

Abaqus, F. E. A. (2009). ABAQUS analysis user's manual. *Dassault Systemes, Vélizy-Villacoublay, France.*

Aguilar, R., Zonno, G., Lozano, G., Boroschek, R., and Lourenço, P. B. (2019). Vibration-based damage detection in historical adobe structures: Laboratory and field applications. *International Journal of Architectural Heritage*, 13(7):1005–1028.

Al Aqtash, U., Bandini, P., and Cooper, S. L. (2017). Numerical approach to model the effect of moisture in adobe masonry walls subjected to in-plane loading. *International Journal of Architectural Heritage*, 11(6):805–815.

Alkayem, N. F., Cao, M., Zhang, Y., Bayat, M., and Su, Z. (2018). Structural damage detection using finite element model updating with evolutionary algorithms: a survey. *Neural Computing and Applications*, 30(2):389–411.

Angjeliu, G., Coronelli, D., and Cardani, G. (2020). Development of the simulation model for Digital Twin applications in historical masonry buildings: The integration between numerical and experimental reality. *Computers & Structures*, 238:106282.

Arto, I., Gallego, R., Cifuentes, H., Puertas, E., and Gutiérrez-Carrillo, M. (2021). Fracture behavior of rammed earth in historic buildings. *Construction and Building Materials*, 289:123167.

Ávila, F., Puertas, E., and Gallego, R. (2022a). Characterization of the mechanical and physical properties of stabilized rammed earth: A review. *Construction and Building Materials*, 325:126693.

Ávila, F., Puertas, E., and Gallego, R. (2022b). Mechanical characterization of lime-stabilized rammed earth: Lime content and strength development. *Construction and Building Materials*, 350:128871.

Azzara, R. M., De Roeck, G., Girardi, M., Padovani, C., Pellegrini, D., and Reynders, E. (2018). The influence of environmental parameters on the dynamic behaviour of the San Frediano bell tower in Lucca. *Engineering Structures*, 156:175–187.

Bernardo, G., Guida, A., and Pacente, G. (2022). The sustainability of raw earth: an ancient technology to be rediscovered. *Journal of Architectural Conservation*, pages 1–13.

Boller, C., Chang, F. K., and Fujino, Y. (2009). *Encyclopedia of structural health monitoring*, volume 2960. Wiley Online Library.

Bui, T. L., Bui, T. T., Bui, Q. B., Nguyen, X. H., and Limam, A. (2020). Out-of-plane behavior of rammed earth walls under seismic loading: Finite element simulation. *Structures*, 24:191–208.

Cabboi, A., Gentile, C., and Saisi, A. (2017). From continuous vibration monitoring to FEM-based damage assessment: application on a stone-masonry tower. *Construction and Building Materials*, 156:252–265.

Carden, E. P. and Fanning, P. (2004). Vibration based condition monitoring: a review. *Structural health monitoring*, 3(4):355–377.

Ceravolo, R., Coletta, G., Miraglia, G., and Palma, F. (2021). Statistical correlation between environmental time series and data from long-term monitoring of buildings. *Mechanical Systems and Signal Processing*, 152:107460.

Chakraborty, S., Adhikari, S., and Ganguli, R. (2021). The role of surrogate models in the development of digital twins of dynamic systems. *Applied Mathematical Modelling*, 90:662–681.

Chiachío, M., Megía, M., Chiachío, J., Fernandez, J., and Jalón, M. L. (2022). Structural digital twin framework: Formulation and technology integration. *Automation in Construction*, 140:104333.

de Oliveira Dias Prudente dos Santos, J. P., Crémona, C., da Silveira, A. P. C., and de Oliveira Martins, L. C. (2016). Real-time damage detection based on pattern recognition. *Structural Concrete*, 17(3):338–354.

Farrar, C. R. and Worden, K. (2012). *Structural health monitoring: a machine learning*

perspective. John Wiley & Sons.
García-Macías, E., Venanzi, I., and Ubertini, F. (2020). Metamodel-based pattern recognition approach for real-time identification of earthquake-induced damage in historic masonry structures. *Automation in Construction*, 120:103389.
García-Macías, E., Ierimonti, L., Venanzi, I., and Ubertini, F. (2021). An innovative methodology for online surrogate-based model updating of historic buildings using monitoring data. *International Journal of Architectural Heritage*, 15(1):92–112.
García-Macías, E. and Ubertini, F. (2020). MOVA/MOSS: Two integrated software solutions for comprehensive Structural Health Monitoring of structures. *Mechanical Systems and Signal Processing*, 143:106830.
García-Macías, E. and Ubertini, F. (2022a). Integrated SHM Systems: Damage Detection Through Unsupervised Learning and Data Fusion. In *Structural Health Monitoring Based on Data Science Techniques*, pages 247–268. Springer.
García-Macías, E. and Ubertini, F. (2022b). Least Angle Regression for early-stage identification of earthquake-induced damage in a monumental masonry palace: Palazzo dei Consoli. *Engineering Structures*, 259:114119.
García-Macías, E. and Ubertini, F. (2022c). Real-time Bayesian damage identification enabled by sparse PCE-Kriging meta-modelling for continuous SHM of large-scale civil engineering structures. *Journal of Building Engineering*, page 105004.
GB 50010-2010 (2010). Code for design of concrete structures. *Standardization Administration of China: Beijing, China.*
Gentile, C., Ruccolo, A., and Canali, F. (2019). Long-term monitoring for the condition-based structural maintenance of the Milan Cathedral. *Construction and Building Materials*, 228:117101.
González Limón, T. and Casas Gómez, A. (1997). Estudio de los materiales y de las fábricas de la Torre de Comares de la Alhambra. Technical report, Biblioteca del Patronato de la Alhambra y Generalife.
Hanif, M. U., Ibrahim, Z., Jameel, M., Ghaedi, K., and Aslam, M. (2016). A new approach to estimate damage in concrete beams using non-linearity. *Construction and Building Materials*, 124:1081–1089.
Hou, R. and Xia, Y. (2021). Review on the new development of vibration-based damage identification for civil engineering structures: 2010–2019. *Journal of Sound and Vibration*, 491:115741.
Jaquin, P. A., Augarde, C. E., and Gerrard, C. M. (2007). Historic rammed earth structures in Spain : construction techniques and a preliminary classification. In *Proceedings of International Symposium on Earthen Structures 2007*. Interline Publishing. Conference details: 22-24 August 2007, Bangalore, India.
Jiménez-Delgado, M. C. and Guerrero, I. C. (2006). Earth building in Spain. *Construction and Building Materials*, 20(9):679–690.
Juang, J. N. (1994). *Applied system identification*. Prentice-Hall, Inc.
Kleijnen, J. P. C. (2009). Kriging metamodeling in simulation: A review. *European journal of operational research*, 192(3):707–716.
Kleijnen, J. P. C. (2017). Regression and Kriging metamodels with their experimental designs in simulation: a review. *European Journal of Operational Research*, 256(1):1–16.
Kung, S. Y. (1978). A new identification and model reduction algorithm via singular value decomposition. In *Proc. 12th Asilomar Conf. on Circuits, Systems and Computers, Pacific Grove, CA, November, 1978.*
Lai, Z., Mylonas, C., Nagarajaiah, S., and Chatzi, E. (2021). Structural identification with physics-informed neural ordinary differential equations. *Journal of Sound*

and Vibration, 508:116196.

Lophaven, S. N., Nielsen, H. B., and Søndergaard, J. (2002). DACE-A Matlab Kriging toolbox, version 2.0. Technical report, Technical University of Denmark.

Martínez, J., Ávila, F., Puertas, E., Burgos-Núñez, A., and Gallego-Sevilla, R. (2022). Historical and architectural study for the numerical modeling of heritage buildings: the Tower of Comares of the Alhambra (Granada, Spain). *Informes de la Construcción*, 74(565):e429.

Martinez-Luengo, M., Kolios, A., and Wang, L. (2016). Structural health monitoring of offshore wind turbines: A review through the statistical pattern recognition paradigm. *Renewable and Sustainable Energy Reviews*, 64:91–105.

Miccoli, L., Gerrard, C., Perrone, C., Gardei, A., and Ziegert, C. (2017). A collaborative engineering and archaeology project to investigate decay in historic rammed earth structures: The case of the medieval preceptory in Ambel. *International Journal of Architectural Heritage*, 11(5):636–655.

Minke, G. (2013). *Building with earth.* Birkhäuser.

Mishra, M. (2021). Machine learning techniques for structural health monitoring of heritage buildings: A state-of-the-art review and case studies. *Journal of Cultural Heritage*, 47:227–245.

Mishra, M., Lourenço, P. B., and Ramana, G. V. (2022). Structural health monitoring of civil engineering structures by using the internet of things: A review. *Journal of Building Engineering*, 48:103954.

Nguyen, T. D., Bui, T. T., Limam, A., Bui, T. L., and Bui, Q. B. (2021). Evaluation of seismic performance of rammed earth building and improvement solutions. *Journal of Building Engineering*, 43:103113.

Pallarés, F. J., Betti, M., Bartoli, G., and Pallarés, L. (2021). Structural health monitoring (SHM) and Nondestructive testing (NDT) of slender masonry structures: A practical review. *Construction and Building Materials*, 297:123768.

Peeters, B. (2000). *System identification and damage detection in civil engineering.* PhD thesis, Katholieke Universiteit, Leuven, Belgium.

Peeters, B. and De Roeck, G. (2001). One-year monitoring of the Z24-Bridge: environmental effects versus damage events. *Earthquake Engineering & Structural Dynamics*, 30(2):149–171.

Reynders, E. and De Roeck, G. (2008). Reference-based combined deterministic-stochastic subspace identification for experimental and operational modal analysis. *Mechanical Systems and Signal Processing*, 22(3):617–637.

Rytter, A. (1993). *Vibrational based inspection of civil engineering structures.* PhD thesis, Aalborg University.

Sacks, J., Welch, W. J., Mitchell, T. J., and Wynn, H. P. (1989). Design and analysis of computer experiments. *Statistical science*, 4(4):409–423.

Schroeder, H. (2016). *The development of earth building.* Springer.

Scozzese, F., Ragni, L., Tubaldi, E., and Gara, F. (2019). Modal properties variation and collapse assessment of masonry arch bridges under scour action. *Engineering Structures*, 199:109665.

Silva, R. A., Mendes, N., Oliveira, D. V., Romanazzi, A., Domínguez-Martínez, O., and Miranda, T. (2018). Evaluating the seismic behaviour of rammed earth buildings from Portugal: From simple tools to advanced approaches. *Engineering Structures*, 157:144–156.

Sobol, I. M. (1967). The distribution of points in a cube and the approximate evaluation of integrals. *USSR Computational Mathematics and Mathematical Physics*, 7:784–802.

Stein, M. L. (1999). *Interpolation of spatial data: some theory for kriging*. Springer Science & Business Media.

Tao, F., Zhang, H., Liu, A., and Nee, A. Y. C. (2018). Digital twin in industry: State-of-the-art. *IEEE Transactions on industrial informatics*, 15(4):2405–2415.

Ubertini, F., Cavalagli, N., Kita, A., and Comanducci, G. (2018). Assessment of a monumental masonry bell-tower after 2016 Central Italy seismic sequence by long-term SHM. *Bulletin of Earthquake Engineering*, 16(2):775–801.

Van Overschee, P. and De Moor, B. (2012). *Subspace identification for linear systems: Theory—Implementation—Applications*. Springer Science & Business Media.

Venanzi, I., Kita, A., Cavalagli, N., Ierimonti, L., and Ubertini, F. (2020). Earthquake-induced damage localization in an historic masonry tower through long-term dynamic monitoring and FE model calibration. *Bulletin of Earthquake Engineering*, 18(5):2247–2274.

Viu, J. M., Fernández, J. R., and Caralt, J. S. (2008). The impact of heritage tourism on an urban economy: the case of Granada and the Alhambra. *Tourism Economics*, 14(2):361–376.

Vuoto, A., Ortega, J., Lourenço, P. B., Suárez, F. J., and Núñez, A. C. (2022). Safety assessment of the Torre de la Vela in la Alhambra, Granada, Spain: The role of on site works. *Engineering Structures*, 264:114443.

Zhou, T. and Liu, B. (2019). Experimental study on the shaking table tests of a modern inner-reinforced rammed earth structure. *Construction and Building Materials*, 203:567–578.

Zhou, X., Kim, C. W., Zhang, F. L., and Chang, K. C. (2022). Vibration-based Bayesian model updating of an actual steel truss bridge subjected to incremental damage. *Engineering Structures*, 260:114226.

Zini, G., Betti, M., and Bartoli, G. (2022). A quality-based automated procedure for operational modal analysis. *Mechanical Systems and Signal Processing*, 164:108173.

Zonno, G., Aguilar, R., Boroschek, R., and Lourenço, P. B. (2019). Experimental analysis of the thermohygrometric effects on the dynamic behavior of adobe systems. *Construction and Building Materials*, 208:158–174.